New Microfabrication Method for Prototyping Integrated Microfluidic Modules with SR-3000 and Polydimethylsiloxane(PDMS)

By

Thomas Frederick Gerlach

RECOMMENDED: Rebasmita Misra

Jiefeng Pan

Kenneth P Roo

Cheng-Hsin Chen

Advisory Committee Chair

John Lee

Chair, Department of Mechanical Engineering

APPROVED:

Dean, College of Engineering and Mines

Laurence K Duffy

Dean of Graduate School

July 31, 2012

Date

New Microfabrication Method for Prototyping Integrated Microfluidic Modules with SR-3000 and Polydimethylsiloxane(PDMS)

A

THESIS

Presented to the Faculty
of the University of Alaska Fairbanks

in Partial Fulfillment of the Requirements
for the Degree of

MASTER OF SCIENCE

By

Thomas Frederick Gerlach, B.S.

Fairbanks, Alaska

August 2012

Abstract

This thesis presents the first work on the fabrication of microfluidic modules with SR-3000 Rayzist photoresist paper and polydimethylsiloxane (PDMS). Chapter 1 of the thesis is on the analysis of elemental composition of SR-3000. By using the X-Ray Fluorescence spectrometer we found the SR-3000 sheet is enriched with silicon, the key element for forming covalent bonding to PDMS. Chapters 2, 3,and 4 of the thesis is focused on the characterization of both the hydrophilicity of the plasma-treated SR-3000 surface and the bonding strength between SR-3000 and PDMS. Unfiltered air was used as the process gas for plasma-assisted bonding of SR-3000 to PDMS. Pressure rupture tests were conducted to measure the strength at the bonding interface, which can be as high as 57.7 psi, strong enough to hold the fluid pressure for typical microfluidics applications. The hydrophilicity of SR-3000 is mainly governed by the plasma treatment time. Chapter 5 demonstrates how to use the developed microfabrication method to prototype microfluidic modules for typical microfluidic applications, which include manipulation of laminar flow, mixing of miscible fluids, and production of oil droplets in a stream of water flow.

Table of Contents Page

Signature Page i

Title Page ii

Abstract iii

Table of Contents iv

List of Figures vi

List of Tables x

Acknowledgements xi

Chapter 1 Introduction to Microfluidics 1

1.1 Overview of Microfluidics 1

1.2 Microfluidic Channel Fabrication Methods 2

1.3 Objective and Structure of Thesis 4

Chapter 2 SR-3000 Surface Element Composition 6

2.1 Introduction to SR-3000 Photoresist 6

2.2 Introduction to X-Ray Fluorescence (XRF) 7

2.3 XRF Equipment 9

2.4 XRF Procedure 10

2.5 XRF Data for SR-3000 Photoresist 12

2.6 Conclusions 14

Chapter 3 SR-3000 to PDMS Bonding by Unfiltered Air Plasma 16

3.1 Introduction 16

3.2 Materials and Equipment Plasma-Assisted Bonding 17

3.3 Determining the Optimal Plasma Oxygenation Bonding Procedure 24

3.4 Rupture Test Procedure 28

3.5 Results and Discussions 30

3.6 Conclusion 35

Chapter 4 Hydrophilicity of Plasma Oxygenated SR-3000 36

4.1 Introduction *36*

4.2 Equipment Used to Determine Contact Angle *37*

4.3 Test Set-up and Contact Angle Measurement Procedure *39*

4.4 Results and Discussions *43*

4.5 Conclusions *48*

Chapter 5 SR-3000-PDMS Microfluidic Demonstrations **49**

5.1 Introduction *49*

5.2 Equipment for Channel Fabrication *49*

5.3 Channel Design and Procedure *53*

5.4 Characterization of Microchannels in SR-3000 ..... *58*

5.5 Prototyping Designs for Demonstrations *63*

5.5.1 Demonstration of Laminar Flow *63*

5.5.2 Demonstration of Water-Water Mixing *66*

5.5.3 Demonstration of Oil Droplet in Water Generation *69*

5.8 Conclusions *73*

Chapter 6 Summary and Suggestions for Future Work **75**

6.1 Summary *75*

6.2 Future Work *75*

References **77**

Appendix **80**

List of Figures **Page**

Figure 1: Microfluidics impact on drug discovery (Dittrich and Manz 2006)..... 1
Figure 2: SolidWorks design of microfluidic device using SR300 and PDMS. 6
Figure 3: XRF compared to other forms of composition identification (Philips Analytical, 2008). . 7
Figure 4: Schematic demonstrating the impact of an X-ray on an atom(Potts, 1986). 8
Figure 5: PANalytical Axios XRF..... 9
Figure 6: SR-3000 Rayzist Photomask (Rayzist Photomask INC., Vista CA). 10
Figure 7: Preparation of SR-3000 samples PANalytical Axios XRF machine. 10
Figure 8: Diagram of components of XRF machine (Philips 2008)..... 11
Figure 9: Compiled XRF data for the smooth side of SR-3000..... 12
Figure 10: Compiled XRF data for the rough side of SR-3000..... 13
Figure 11: The oxidization process on the surface plasma treated PDMS (Owen, M.J. and Smith, P.J. 1994)..... 15
Figure 12: SR-3000 Rayzist Photomask (Rayzist Photomask INC., CA). 17
Figure 13: Sylgard 184 Silicon Elastomer Kit (Dow Corning Corp., MI)..... 18
Figure 14: My Weigh i201 Digital Scale (My Weigh, British Columbia). 18
Figure 15: Fisher Scientific Vacuum Chamber (Thermo Fisher Scientific, MA)..... 19
Figure 16: Schmidt Press MHPM-UNV with 0.023 inch Hole Punch (Schmidt Technology Corp., PA)..... 19
Figure 17: Harrick Plasma (NY) Plasmaflow PDC-FMG and Plasma Cleaner PDC-32G. 20
Figure 18: Oerlikon Corp.(Switzerland) Trivac D2,5E vacuum pump..... 20
Figure 19: Samsung Galaxy S2(South Korea) Stop Watch Application. 21
Figure 20: Corning Inc. (NY) PC-620D hot plate..... 21
Figure 21: KCD IP LLC. (IL) Craftsman air compressor..... 22
Figure 22: Watts (MA) hex nipple and pipe tee..... 22
Figure 23: Gorilla Glue Company's (OH) Gorilla Glue. 22
Figure 24: Teqequipment Net (NJ) Fluke pressure transducer module and multi-meter. 23
Figure 25: Ningbo Changqui Fluorine Plastic Products Co., Ltd.'s, (China) CFPC thread seal tape. 23
Figure 26: Itronix Inc. (CA) rounded tip stainless steel probes..... 23
Figure 27: VWR Labshop, (IL) Tygon plastic tubing..... 24
Figure 28: PDMS in aluminum pressure mold. At the center of the mold the protruded cylinder is to replicate the pressure chamber for testing the bonding strength..... 25
Figure 29: SolidWorks drawing of SR-3000 PDMS bonding test sample. (Dimensions in inches).25
Figure 30: Samples in vacuum desiccator for degassing and oven for curing. 26
Figure 31: PDMS in hole press. 26
Figure 32: 3mm x 3mm SR-3000 being washed with warm water for 1 minute and 30 seconds. 27
Figure 33: Samples after testing and SolidsWorks close up of sample. 28
Figure 34: Set up prior to pressure rupture test..... 29

Figure 35: A sample just ruptured in the rupture testing. 29
Figure 36: 200 mTorr rupture pressure test data graphically varying different plasma treatment parameters of treatment time and power. 31
Figure 37: 300 mTorr rupture pressure test data graphically varying different plasma treatment parameters of treatment time and power. 32
Figure 38: Samples after rupture pressure test. 33
Figure 39: First mode of failure between SR-3000 and PDMS bond. 33
Figure 40: Second mode of failure between SR-3000 and PDMS bond. 34
Figure 41: Third mode of failure between SR-3000 and PDMS bond. 34
Figure 42: Contact angle measurement system set up. 36
Figure 43: TDI International Tweezers 2A-SADH (Switzerland). 37
Figure 44: Accu-Scope 3030 Microscope series (NY). 38
Figure 45: 10mL HSW syringe (America) 38
Figure 46: Photron Fastcam PCI R2 (CA). 39
Figure 47: Roting Architectural Protractor (Germany). 39
Figure 48: Sample #47 with noted droplet placements. 40
Figure 49: Sample placed in plasma chamber. 40
Figure 50: Sample in the microscope. 41
Figure 51: Droplet produced by syringe. 41
Figure 52: Close up view through microscope focused on contact angle. 42
Figure 53: Protractor measuring contact angle. 43
Figure 54: Sample #14 Droplet Change From 0-5 Minutes. Pressure=207 mTorr, Power= 18 W, and Treatment Time= 40 seconds. 44
Figure 55: 200 mTorr Contact Angle Data Graphically. The filled in marks represents the contact angle at 0 seconds and the open mark is the contact angle at 30 seconds. 46
Figure 56: 300 mTorr Contact Angle Data Graphically. The filled in marks represents the contact angle at 0 seconds and the open mark is the contact angle at 30 seconds. 47
Figure 57: SR-3000 Rayzist Photomask (Rayzist Photomask INC., Vista CA). 50
Figure 58: UV Vellum printed with channel patterns cut. 50
Figure 59: Ikonics Imaging Letralite black light (MN). 51
Figure 60: Spraying Systems Co. Trigger Jet Hand sprayer (150 max psi) (IL). 51
Figure 61: SR-3000 wash out board with magnetic strips. 52
Figure 62: Advance Chemical Engineering Acextra Magic Dark Spray (CA) with applicator. 52
Figure 63: Schematic of SR-3000 channel wash out process. 53
Figure 64: Channel pattern printed onto UV Vellum at 1200 dpi. 54
Figure 65: Comparison of a patterned printed on vellum sheet. A. Printed channel without the application of Magic Dark. B. Printed channel with an application of Magic Dark. 54
Figure 66: SR-3000 film rough matte side up underneath the Letralite black light with the printed side of the UV vellum against the rough side of the SR-3000. 55

Figure 67: SR-3000 and channel pattern being wrapped in the Letralite blanket before being placed over the black light. 56
Figure 68: SR-3000 sheet prepared for washout. 56
Figure 69: Hand sprayer at the appropriate distance from the SR-3000 film during wash out. 57
Figure 70: SR-3000 after successful channel washes out. 58
Figure 71: SEM produced channel profile. A: The cross-section. B: Run-through. 59
Figure 72: Traditional microscope produced channel profile at 60x. A: Cross-sectional view. B: Run-through view. 60
Figure 73: Top down view of channel walls at 60x zoom. Left: SR-3000 PDMS Microchannel. Right: PDMS-PDMS Microchannel. 61
Figure 74: Top down view of channel walls at 120x zoom. Left: SR-3000 PDMS Microchannel. Right: PDMS-PDMS Microchannel. 61
Figure 75: Top down view of channel walls at 200x zoom. Left: SR-3000 PDMS Microchannel. Right: PDMS-PDMS Microchannel. 62
Figure 76: Top down view of channel walls at 400x zoom. Left: SR-3000 PDMS Microchannel. Right: PDMS-PDMS Microchannel. 63
Figure 77: Dog bone channel design to demonstrate laminar fluid flow. 0.75pt line width. 64
Figure 78: Oil and water flows meet at the Y-junction of channel (at 120x magnification). 65
Figure 79: Oil and water laminar fluid flow in channel at 60x magnification. (a) Fluid flow 5cm from the Y-junction. (b) Fluid flow 10 cm from the Y-junction. 66
Figure 80: Diagram of diffusive mixing (System Biology Intro Lecture, 2008). 67
Figure 81: Mixing channel design. 0.75pt line width. 68
Figure 82: Blue and Yellow dyed water entering the Y-Junction displaying laminar flow. 68
Figure 83: Mixing channel after 10 minutes of fluid flow, note the color pallet shifting from blue on left to green in middle to yellow on the right. 69
Figure 84: T-Junction Channel design to produce oil droplets in a water flow. 0.75pt width. 70
Figure 85: Oil droplet moving in a working fluid of water. 71
Figure 86: Oil droplets of varying size moving through a working fluid of dyed water. 72
Figure 87: Beginning of the formation of a droplet plug of oil in water. 72
Figure 88: Droplet plug fully developed down channel. 73
Figure 89: XRF Scan 1 data 80
Figure 90: XRF Scan 2 data 81
Figure 91: XRF Scan 3 data 82
Figure 92: XRF Scan 4 data 83
Figure 93: XRF Scan 5 data 84
Figure 94: XRF Scan 6 data 85
Figure 95: XRF Scan 7 data 86
Figure 96: XRF Scan 8 data 87
Figure 97: XRF Scan 9 data 88

Figure 98: XRF Scan 10 data 89

List of Tables **Page**

Table 1: Contact angle measured right when the droplet was placed on the SR-3000 surface which was plasma treated by the corresponding parameters. 45
Table 2: Contact angle measured 30 seconds after the droplet was placed on the SR-3000 surface which was plasma treated by the corresponding parameters. (The data in Table 1 and Table 2 are compiled into Table 7 in the Appendix). 45
Table 3: Fluid flow rates for laminar flow. 65
Table 4: Mixing channel fluid flow rates. 69
Table 5: Droplet plug fluid flow rates. 73
Table 6: Plasma bonding strength results 90
Table 7: Contact angle date for zero and 30 seconds after placing on the surface 91

Acknowledgements

The author would like to express his gratitude toward Dr. Cheng-fu Chen for his continued advice and support as the committee chair and graduate advisor, and committee members Dr. Jifeng Peng, Dr. Debasmita Misra and Dr. Kenneth Severin for their guidance. I thank Dustin Ray and Yanhong (Jenny) Gu for helping with use of the SEM and XFR data analysis. The author would also like to thank Dr. Robert Gerlach, Dr. Rosemarie Lombardi, Annemarie Gerlach, Mark Kurpinski, John and Jane Jones, Jerry and Carol Morris, Robert Schnell, and all his family and friends for their continued encouragement and guidance through the years.

Chapter 1 Introduction to Microfluidics

1.1 Overview of Microfluidics

In recent years, microfluidics has been increasingly studied in numerous multidisciplinary fields, ranging from engineering to biological applications. This relatively new field of study involves working to control milliliter to nanoliter volumes of fluid in mircrofluidic channels. A long term goal of microfluidics is to develop different channel designs that will allow for the synthesis of different cures for diseases at a faster rate and common biological test to be done with less fluid, thus reducing the need for a variety of different large lab equipment (see Figure 1). By using such minute volumes of reagents, reaction times are drastically reduced and only a fraction of the lab space is required (Teh, Lin, Hung, & Lee, 2008).

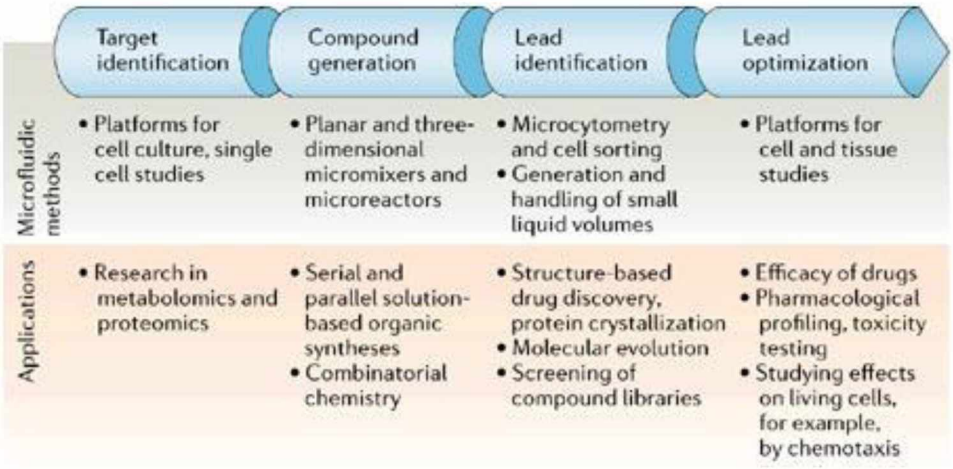

Figure 1: Microfluidics impact on drug discovery (Dittrich and Manz 2006).

The integration of an entire lab facility into a device similar in size to a computer chip is the holy grail of microfluidics. This integration could be the first step in proper prevention and treatment of diseases that do not currently have accurate diagnostic techniques. Another need for these microfluidic devices is to create a low cost diagnostic tool. Diagnosis technologies that are successful in an economically developed world are often difficult to apply to developing countries. The people of these developing countries frequently cannot afford even modestly priced tests, and basic infrastructures such as reliable power, refrigeration, and trained personnel. Most diagnosis needs to be completed by a trained healthcare worker to recognize

symptoms or interpret analysis. The emergence of new and effective diagnosis technologies for developing countries could allow for better treatment of diseases in areas without access to trained medical personnel (Baroud, Gallaire, & Dangla, 2010).

Another application of microfluidic devices is the creation of droplets. Micro-sized droplets have recently caught the attention of many researchers for their numerous and diverse applications that advance expanding scientific fields and emerging technologies. Micro droplets have already shown great potential as ultrasound contrast agents, therapies for thrombus destruction, and new targeted drug delivery. In all of these applications, the droplet size and distribution are important parameters of a gas–liquid flow in T-junction microfluidic devices (J. Tan, Li, Wang, & Luo, 2009). Droplet-based microfluidics is still in its infancy, and there are many opportunities to research methods for making microfluidic modules practical, genuinely useful, and to expand their capabilities. Since this is such a new technology, there is still a huge need for detailed studies that could help improve the design of the devices, which may propose new capabilities for these devices. Additionally, the development of new methods for fabricating microfluidic modules and the development of new components such as electrodes, valves, filters, mixers, and coatings for microfluidic modules will also expand their capabilities (Duffy, McDonald, Schueller, & Whitesides, 1998).

1.2 Microfluidic Channel Fabrication Methods

The research in microfluidics has seen rapid development in new methods of fabrication— to prototype elements such as microchannels, valves, mixers, and pumps that are essential elements of microchemical 'factories' on a chip. There are currently several different methods to prototype microfluidic channels such as photolithography, soft lithography, and Shrinky Dinks. Each of these approaches has different advantages. For example, soft lithography shares common processes with photolithography, but does not require expensive and brittle components. Soft lithography uses polydimethylsiloxane (PDMS) as the structural material for prototyping microfluidic devices. Although photolithography is the most costly and time consuming method of creating channels, it can provide the most precise and confined design for making microfluidic devices with smaller features (Bender, 2011). Shrinky Dinks is a toy, it just happens that the material used in Shrinky Dinks can be used in soft lithography. Using Shrinky Dinks greatly cuts costs of expensive materials and process in photo lithography. However, the problem with Shrinky Dinks is that they tend to produce inconsistencies in prototyping.

Photolithography develops channels out of silicon, glass, or quartz. Although these materials have beneficial material properties, the complex and expensive process required to develop intricate channels can be economically taxing. Special equipment is needed to perform operations on these materials, which generally requires a clean room facility. The maintenance

and cost of lab equipment and facilities makes photolithography more expensive than other microchannel fabrication methods (Bender, 2011).

Some of the most important contributions are seen in the development of soft lithography by introducing PDMS as the structural material for fabricating prototype devices. PDMS allows for fabricating pneumatically activated valves, mixers and pumps. Among a few fabrication techniques in the broader perspective of soft lithography (Xia & Whitesides, 1998), polymeric replication of the inverse patterns on a master mold and direct printing are two well-applied approaches for prototyping microfluidic modules. In the development of molding techniques in soft lithography, high-precision molds made of SU-8 photoresist are lithographically prepared, but costly. The demand for replicating polymeric microfluidic components in low-cost molds has inspired a variety of fast prototyping methods. Examples include the early work of using printed transparencies to replace chrome masks (Duffy et al., 1998) direct printing of laser toner onto transparencies (Y. Tan, Cristini, & Lee, 2005); and the recent Shrinky-Dink microfluidics. On the other end, open channels patterned on the SU-8 photoresist can be directly sealed to PDMS substrates by chemical bonding via the amine-epoxide reaction (Murakami Kuroda, & Osawa, 1998). However, this bonding process requires N_2 plasma treatment on PDMS and thermal treatment at 150°C for 24 hours. Nevertheless, these methods have made it possible to fabricate prototype devices for testing new ideas in a time period much shorter than that which could be achieved using photo lithography, which for non-specialists is a month or more (Duffy et al., 1998).

Recently, Shrinky Dinks microfluidics has become a popular method for producing microfluidic channels due to its low cost and accessibility. In this method designs are printed onto a Shrinky Dink thermoplastic sheet. This sheet is then baked, shrinking its size to about 63% of its previous dimensions. The Shrinky Dink sheet is then used as a mold for the common microchannel material of PDMS (Jablonski, 2009). This fabrication breakthrough has been confronted with both praise and skepticism from the scientific community and it's not without issues (Jablonski, 2009). Channels produced with Shrinky Dinks tend to be rougher than those produced by photolithography or other soft lithography methods. The rough profile in a microchannel has a large impact in controlling fluids in operation.

This research introduces a new fabrication technique as an alternative fast- prototyping method for prototyping microfluidic channels. The key is on the identification and development of micro-fabrication onto commercially available photoresist SR-3000 (Rayzist, Vista, CA). This thesis will show that the fabrication cycle of making a workable microfluidic channel can be less than 3 hours and conducted without access to clean room facilities.

1.3 Objective and Structure of Thesis

The objective of the thesis is to develop a new rapid micro-fabrication method for prototyping microfluidic channels at low cost. This method is explored using a new material SR-3000. SR-3000 is a trademark for a photoresist paper created and manufactured by Rayzist (Vista, CA), which is currently used as a stencil mask for the sand-carving industry. This thesis focuses on how SR-3000 is suitable for microfluidics applications. Introducing this new material creates several essential questions about the feasibility of SR-3000 as a good material candidate for prototyping microfluidic modules including:

- With plasma-assisted bonding, is SR-3000 bondable to PDMS, to form an integrated assembly without any fluid leakage concern?
- What is the bonding strength of the SR-3000 to PDMS bonding interface, and what are the best plasma treatment parameters for achieving strong bonding?
- What is the characteristic of working fluids such as deionized water interacting with the SR-3000 sheet?
- Are microchannels made of SR-3000 feasible to perform typical microfluidics applications?

These questions will be answered in this thesis where a novel microfabrication method is presented on the use of SR-3000 photoresist as the structural material for microfluidic applications.. The thesis outline is as follows. In Chapter 1, a literature review of microfluidics was conducted, with an emphasis on fabrication methods without access to clean room facilities and the bonding techniques. SR-3000 (Rayzist Inc, Vista, CA) was then introduced as a new structural material for microfluidics. Beginning with the X-Ray Fluorescence (XRF) analysis of SR-3000, in Chapter 2 the suitability of SR-3000 for plasma bonding to Polydimethylsiloxane (PDMS) is determined. In Chapter 3, a plasma bonded rupture test was conducted to quantify the bonding strength between the SR-3000 and PDMS under a variety of plasma treatment parameters including the treatment time, vacuum pressure and the power at which the plasma is produced. The goal was to find the optimal combination of parameters for the highest possible strength of SR-3000 to PDMS bonding. In Chapter 4, the surface hydrophilicity of SR-3000 was characterized. Droplets of deionized water were placed on the surface of plasma treated SR-3000, and then the contact angle of each droplet on the surface of each SR-3000 sample was measured to find a correlation to the bonding strength. Chapter 5 demonstrated SR-3000's feasibility as a good structural material for making microfluidic modules. Three microfluidic devices were prototyped to demonstrate the operation of laminar flow, mixing, and

droplet production in microchannels. The content of this work was concluded and suggestions for future work are made in Chapter 6.

Chapter 2 SR-3000 Surface Element Composition

2.1 Introduction to SR-3000 Photoresist

SR-3000 is a trademark name for a photoresist paper, created and manufactured by Rayzist (Vista, CA). To date, its sole application has been to serve as a stencil mask for the sand carving industry. SR-3000 sets itself apart from other sand carving stencils as a high-resolution photoresist with an inherent self sticking feature, which allows for finer detail and deeper etches in glass while sand blasting. It is currently produced in 3, 4 and 5-millimeter thicknesses on 11" x 14" sheets. Each of these sheet thicknesses has different strengths; depending on the design being created, different millimeter thicknesses are recommended. The 3mm (i.e., SR-3000) is recommended for fine detailed artwork and half-toned photos, the 4-mil sheet is recommended for moderate detailed artwork, and 5-mil sheet is recommended for bold artwork. These features inspired the research work presented here, as the reported film thickness in these photoresist papers just fit in the regime of applications in microfluidics. Figure 2 outlines one hypothetical design, which is an application of SR-3000 photoresist as a new structural material for microfluidics applications.

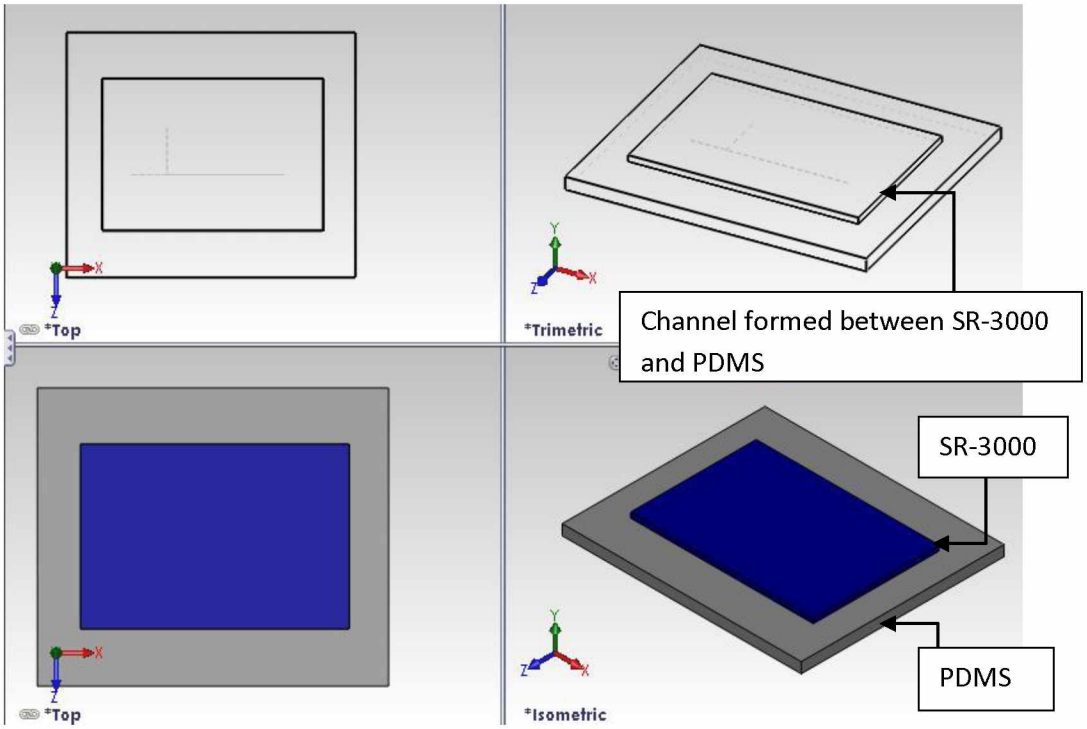

Figure 2: SolidWorks design of microfluidic device using SR300 and PDMS.

In the schematic design, SR-3000 is used to fabricate microchannels and then bonded to PDMS. If successful, this approach would eliminate the use of a molding master as is used in the conventional micro fabrication techniques, thus reducing the preparation time and cost. We hypothesize that the SR-3000, after plasma treatment, would form a similar Si-O backbone as PDMS's, while the oxygen in SR-3000 and from the environment would form the -OH side chain for covalent bonding to PDMS. However there is one issue with this material, which is that there is no information publically available regarding the chemical composition of this photoresist. In order to understand if SR-3000 is bondable to PDMS, we detail an XRF analysis of its elemental composition in Chapter 2. The ability to bond will be primarily dependent on the existence of the element silicon on SR-3000. Silicon is key to the plasma bonding to PDMS, which will be elaborated in Chapter 3.

2.2 Introduction to X-Ray Fluorescence (XRF)

Among a variety of different methods to determine the surface composition of a material, X-ray Fluorescence (XRF) spectrometry is one available at the University of Alaska Fairbanks. XRF scans over a large chemical concentration range, which can be seen in Figure 3. The XRF machine highly automated, which features small errors and high sensitivity. It allows for very small relative statistical errors as low as 0.1-0.3%, meanwhile gathering data on the level of parts per millionth (ppm) (Philips Analytical, 2008). The XRF technique is one of the most widely used routine instrumentation methods of analyzing samples for major elements such as Na, Mg, Al, Si, P, K, Ca, Ti, Mn, Fe. Given the properties of XRF as an analysis tool, it suffices to facilitate the goal of finding silicon in SR-3000, which was the initial hypothesis before conducting the analysis.

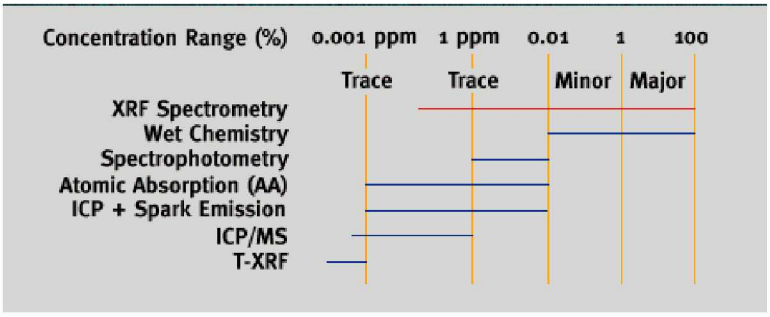

Figure 3: XRF compared to other forms of composition identification (Philips Analytical, 2008).

XRF has been widely applied in geochemistry and forensic science fields (Philips Analytical, 2008). As a complete description of x-ray fluorescence is beyond the scope of this thesis (for more detail see, Potts, 1992, A handbook of silicate rock analysis), what follows is a simplified description:

Electrons are bound to atoms in shells with specific energies, and the energy of those shells is primarily dependent on the number of protons in the atom. To a first order, the differences in energies between shells are also dependent on the number of protons in the atom. When an atom receives sufficient energy, as when it is exposed to x-rays from the tube of the XRF, it can have an inner shell electron removed. The atom will then transition to a lower energy state by having an outer shell electron "move" to the vacant inner shell, and in the process can emit a photon which has the energy equal to the difference between the two shells (Figure 4).

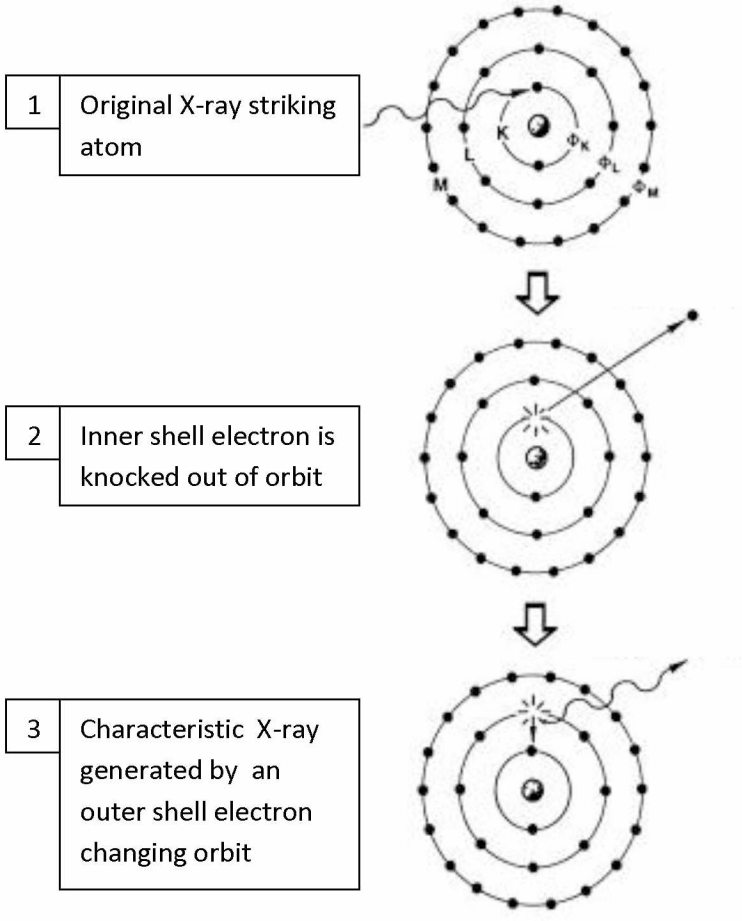

Figure 4: Schematic demonstrating the impact of an X-ray on an atom(Potts, 1986).

The energy of this photon can be related to the number of protons in the atom (atomic number), and thus to a specific element. The number of photons of a given energy can be related to the number of atoms of a given element present in the sample.

In the Axios XRF, the wavelength (which can be directly related to energy) of the emitted photons is measured by scattering them off a diffracting crystal. Several different crystals are used to cover a wider energy range. In this manner a spectrum of the x-rays emitted from the sample can be created. Peaks in the spectrum can be related to specific elements, and the relative height of the peaks is somewhat proportional to the relative abundance of the elements.

2.3 XRF Equipment

To conduct the XRF analysis a PANalytical Axios analyzer was used along with a sample of the SR-3000 samples purchased from Rayzist Photomask INC. (Vista, CA) (see Figure 5 amd Figure 6.)

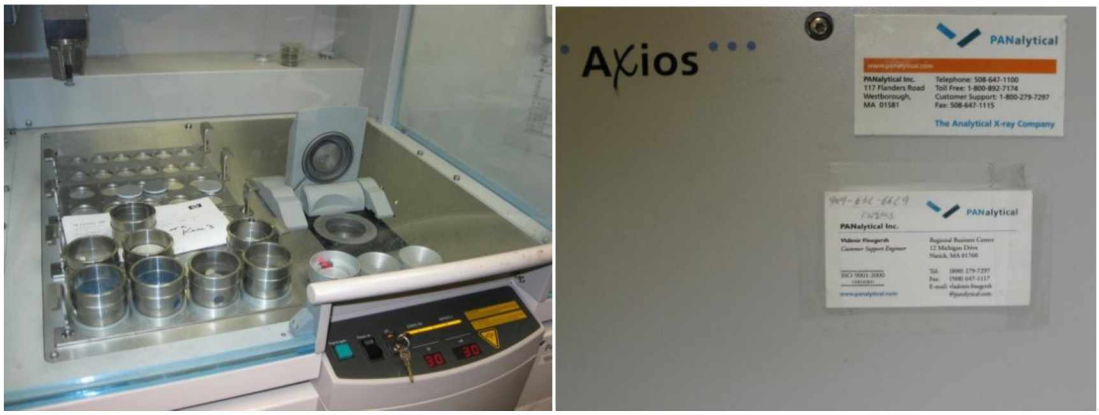

Figure 5: PANalytical Axios XRF.

Figure 6: SR-3000 Rayzist Photomask (Rayzist Photomask INC., Vista CA).

2.4 XRF Procedure

To determine the chemical composition of the two sides of the SR-3000 sheet, two SR-3000 samples were used in the XRF for analysis. One side of the SR-3000 photoresist paper is rough, on which stencil patterns are made out of as per the material usage guideline from the vendor; while the other side is smooth, which is unable to be developed and thus used as a supportive substrate for the paper during the development process. The samples shown in Figure 7 are held in the specimen container with the surface of interest facing downward.

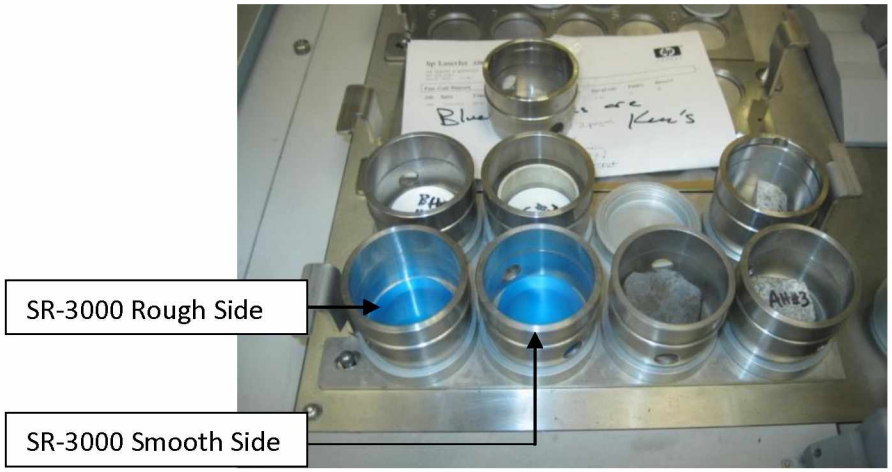

Figure 7: Preparation of SR-3000 samples PANalytical Axios XRF machine.

Figure 8 presents a simplified diagram of the XRF. The sample was exposed to x-rays, causing ionizations as shown in Figure 4. The x-rays that result from these ionizations are diffracted of an analyzing crystal into a detector. Collimators are used to constrain the scattering geometry for better wavelength (and therefore energy) resolution. The specimen-crystal-detector geometry is used to determine the wavelength (and energy) of the emitted x-rays. The number of x-rays at each wavelength/energy is recorded by the XRF. The wavelengths/energies are characteristic of the elements in the sample and the number of x-rays of a given energy is related to the abundance of that element in the sample (Figure 4). After the scanning is completed, the sample is removed from the machine having sustained a little heat damage.

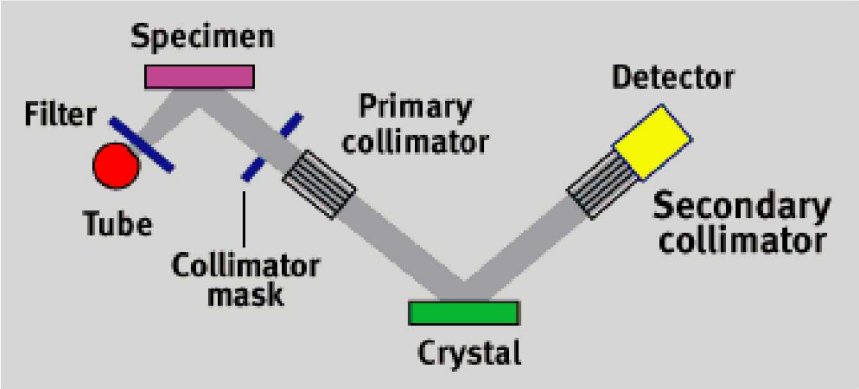

Figure 8: Diagram of components of XRF machine (Philips, 2008).

2.5 XRF Data for SR-3000 Photoresist

The XRF analysis generated ten different scans for both sides (Appendix). The ten scans were compiled into two different graphs to simplify the view and allowed for easier comparison of elemental composition. The compiled scan data are shown in Figure 9 and Figure 10 for the smooth and rough sides, respectively. It is also noted that the XRF analysis was conducted on dry SR-3000 sample, although the SR-3000 should be wetted prior to plasma treatment and bonding to PDMS (cf. Chapter 4). There are two reasons for using dry samples under XRF scanning. The first reason is to eliminate any possible chemical reaction of water with the elements in SR-3000. Second, the SR-3000, once wetted, becomes adhesive.

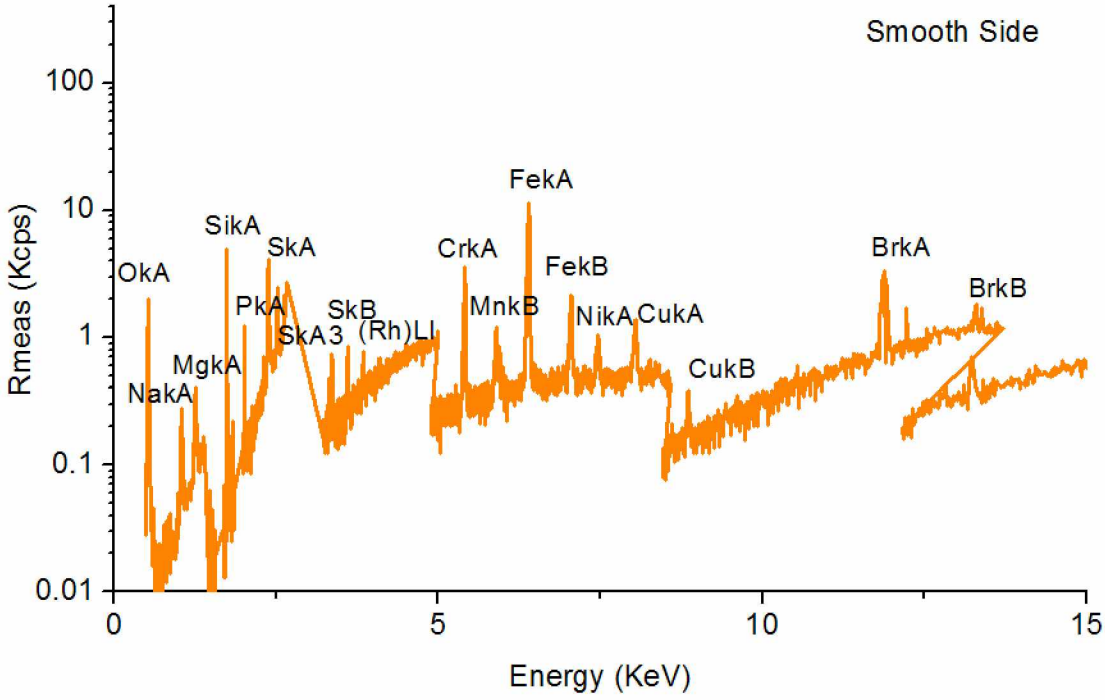

Figure 9: Compiled XRF data for the smooth side of SR-3000.

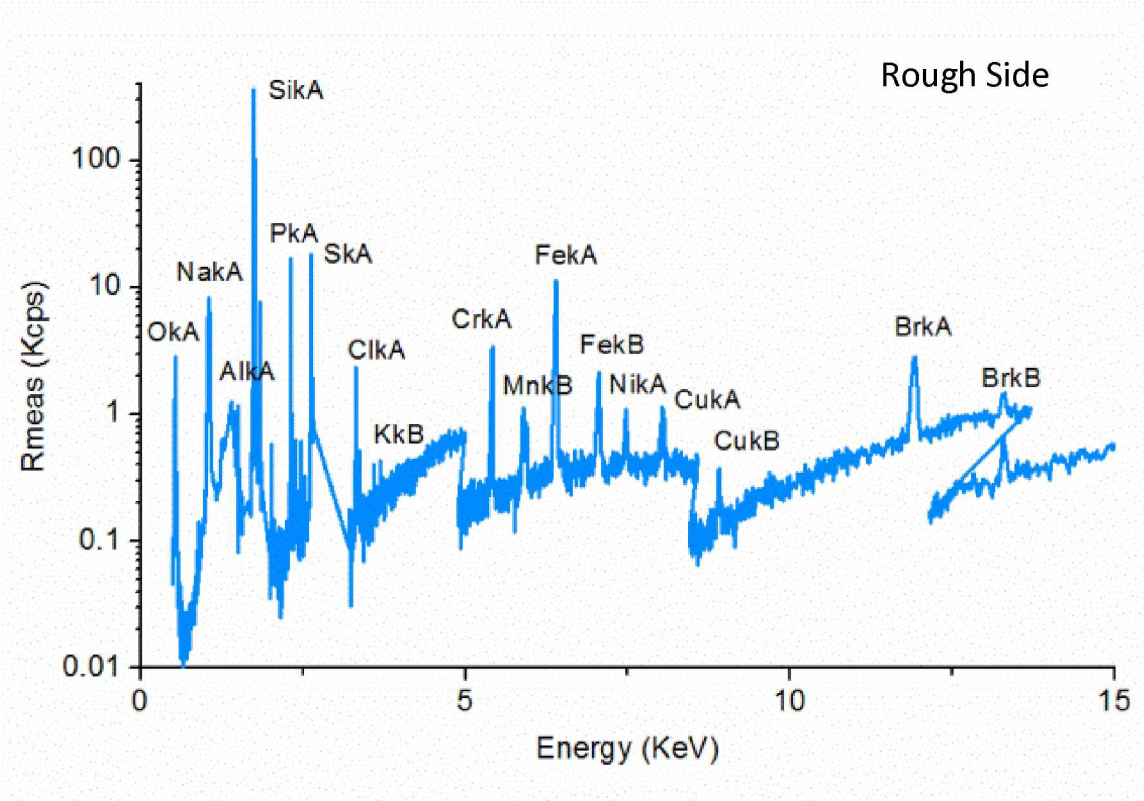

Figure 10: Compiled XRF data for the rough side of SR-3000.

The x-axis represents the energy of the characteristic x-rays emitted by the atoms in the sample, the y-axis represents the number of x-rays emitted. Some elements produce multiple peaks in the spectra because transitions between several shells are possible. While it is tempting to directly correlate the number of x-rays with elemental abundance (twice as many x-rays implies twice as abundant), this is only crudely possible because of variations in excitation and detection efficiencies, and as well as x-ray absorption within the sample itself (Potts, 1992). The rough side has ten times the number of Si related photons; there must be significantly more Si on the rough side than on the smooth side. In Figure 9 and Figure 10 we labeled both for completeness.

A point of interest between the two figures is that the contents of various elements are different from one side to the other of the SR-3000. The rough side contains a substantially larger amount of Potassium, Chlorine, Bromine, and Aluminum, as oppose to the trace amounts found on the smooth side. Additionally, Oxygen is found on both sides, which can play a key role in the plasma assisted bonding of SR-3000 to PDMS. The most important result generated from the XRF analysis is that there are large quantities of Silicon on both the rough and smooth sides of SR-3000. This finding is a key to identifying SR-3000 as a good candidate for the structural material for making microfluidic modules. The finding of Silicon suggests that plasma bonding of

SR-3000 and polymeric organosilicon compound polydimethylsiloxane (PDMS) would be feasible.

2.6 Conclusions

Two samples of SR-3000, one representing the rough side and the other representing the smooth side, were placed into a PANalytical Axios XRF analyzer. This XRF analysis was conducted on the surface of SR-3000 to find its chemical composition and ensure it could be plasma bonded to PDMS.

The graphs produced by the Axios XRF spectrometer software, were able to analyze the content of the rough side surface composition of the SR-3000. Figure 10 shows that there are large amounts of Silicon (Si) on the rough side of SR-3000.

The large amount of Silicon found on the rough surface of the SR-3000 suggests a possibility of plasma assisted bonding of SR-3000 to PDMS. Figure 11 schematically shows the principle of how plasma-assisted bonding occurs in PDMS. In principle, when PDMS is under plasma treatment, oxidation will take place on the surface of the O-Si$(CH3)_2$-enriched polymer to develop the hydroxyl groups (–OH) which are associated with either $SiCH_2OH$ or SiOH (Hollahan & Carlson, 1970). Once the hydroxyl groups are formed on the surface, PDMS is ready for covalent bonding to other similar or dissimilar materials having additional hydroxyl groups through a dehydration reaction (Hollahan & Carlson, 1970). The experiment results show that the SR-3000 photoresist sheet can be bonded to PDMS permanently, which is believed to be from covalent bonding between the hydroxyl groups. However, verification of the bonding mechanism is out of the focus of this thesis. One suggestion to the future work would be that that the SR-3000, after plasma treatment, would form a similar Si-O backbone as PDMS's, while the oxygen in SR-3000 and from the environment would form the -OH side chain for covalent bonding to PDMS (Further detailed in Figure 11 on the next page).

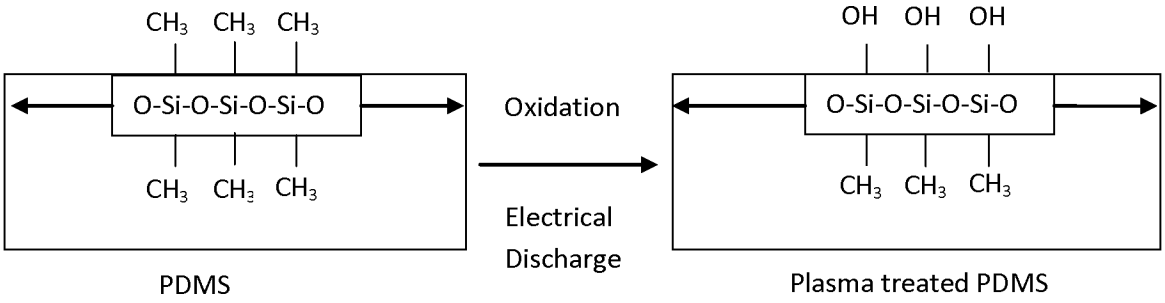

Figure 11: The oxidization process on the surface plasma treated PDMS (Owen, M.J. and Smith, P.J. 1994).

PDMS has become, in recent years, a standard structural material for microfluidic channels. In developing soft lithography PDMS has been widely used, since it allows ideas to be converted to devices with turn-around time much less than those characteristic of conventional silica micromachining (Sia & Whitesides, 2003). Therefore, it is critical to show the ability of the SR-3000 photoresist to be bonded to PDMS. This will allow SR-3000 photoresist to be integrated into the soft lithography and existing microfabrication techniques for developing microfluidic modules. From the XRF analysis we conclude that there is a potential for bonding SR-3000 and PDMS. This is the first major finding in the thesis.

Chapter 3 SR-3000 to PDMS Bonding by Unfiltered Air Plasma

3.1 Introduction

PDMS is made by mixing a silicone resin with a cross-linking agent (composed of dimethylhydrogen siloxane) typically at a 10:1 ratio respectively (Dow Corning Corporation, 2011). PDMS is a commonly used material in microfluidics because it is relatively inexpensive, biocompatible, easily moldable, and can be rapidly produced (The et al., 2008). It also allows for easy viewing in a microscope, as it is optically transparent down to a wavelength of 280 nm (Tang,mLiao, Ong, Wong, Agarwal, Nagarajan, & Yobas, 2006). PDMS also has a high gas permeability, which gives it similar features to a plethora of cellular biological applications (J. Tan, Li, Wang, & Lou, 2006).

Oxygen plasma assisted bonding of PDMS to PDMS and to other heterogeneous materials has been prevalent in prototyping microfluidics since its inception in 1998 (Duffy et al., 1998). When the surface of PDMS is oxygenated, the hydroxyl groups (-OH) will be converted from the O-$Si(CH_3)_2$ group for a limited time (Tang et al., 2006). Once formed, the hydroxyl group on the PDMS surface is ready for covalent bonding to other similar or dissimilar materials having additional hydroxyl groups that are generated through a dehydration reaction to the plasma. A covalent bond is then formed which is so strong that the two pieces become permanently bonded. It only takes between 10-40 seconds of oxygen plasma treatment to produce the needed silanol groups for bonding (Tang et al., 2006; Mark A. Eddings, 2008; Robert White, 2007). After the PDMS is exposed to plasma, it is important to act quickly in joining PDMS pieces to ensure the strongest bond can be formed. A clean environment along with surface of PDMS is necessary as to not contaminate the bonding surface; otherwise the bonding strength would be decreased.

Plasma treatment is also important as it changes the surface of PDMS from being hydrophobic to hydrophilic. Hydrophilic channels become wet very easily, while hydrophobic channels prohibit aqueous water from spreading. Manipulation of the hydrophilicity feature in microfluidics allows for passive control of fluid motion. This property supports electro-osmotic pumping, allowing high surface energy liquids (primarily water) to easily fill the channels (Martinez, Phillips, & Whitesides, 2010).

This chapter presents the first work on the bonding of SR-3000 to a PDMS substrate. As the SR-3000 will be used as the structural material, in conjunction with the PDMS substrate, as for microfluidics devices good bonding strength is needed to contain the pressure generated in microchannels for typical microfluidics applications (Unger, Chou, Thorsen, Scherer, & Quake, 2000). The goal of the bonding test is twofold; to find the optimal plasma-based bonding

parameters, and to measure the bonding strength between the SR-3000 photoresist and the PDMS substrate.

3.2 Materials and Equipment Plasma-Assisted Bonding

This section outlines the equipment and materials used for bonding the SR-3000 photoresist paper to PDMS. The materials include SR-3000 photoresist paper and PDMS. SR-3000 (Figure 12) was purchased from Rayzist Photomask INC. (Vista, CA). Sylgard 184 silicon elastomer kit (Figure 13) was purchased from Dow Corning Corp. (MI) for producing PDMS.

A variety of devices were used to conduct the bonding; they include a digital scale (Figure 14), a desiccator (Fisher Scientific, MA, Figure 15), and a hole punching machine (Schmidt-Technology Corp, PA, Figure 16).

Figure 12: SR-3000 Rayzist Photomask (Rayzist Photomask INC., CA).

Figure 13: Sylgard 184 Silicon Elastomer Kit (Dow Corning Corp., MI).

Figure 14: My Weigh i201 Digital Scale (My Weigh, British Columbia).

Figure 15: Fisher Scientific Vacuum Chamber (Thermo Fisher Scientific, MA).

Figure 16: Schmidt Press MHPM-UNV with 0.023 inch Hole Punch (Schmidt Technology Corp., PA).

The equipment used to complete the plasma bonding include: a Harrick Plasma (NY) Plasmaflow PDC-FMG and Plasma Cleaner PDC-32G, an Oerlikon Corp. (Switzerland) Trivac D2, 5E vacuum pump, an Samsung Galaxy S2 Stop Watch (South Korea), and a Corning Inc. (NY) PC-620D hot plate (Figure 17, Figure 18, Figure 19, Figure 20).

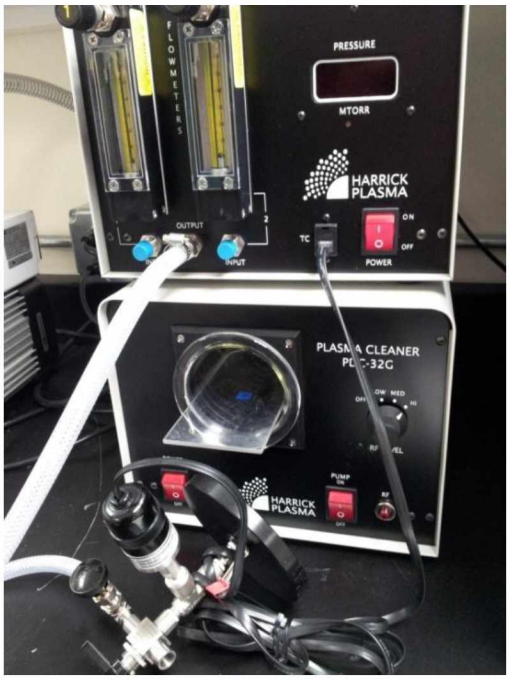

Figure 17: Harrick Plasma (NY) Plasmaflow PDC-FMG and Plasma Cleaner PDC-32G.

Figure 18: Oerlikon Corp.(Switzerland) Trivac D2,5E vacuum pump.

Figure 19: Samsung Galaxy S2(South Korea) Stop Watch Application.

Figure 20: Corning Inc. (NY) PC-620D hot plate.

The rupture pressure was measured with a KCD IP LLC. (IL) Craftsman air compressor, a Watts (MA) hex nipple and pipe tee, Gorilla Glue Company's (OH) Gorilla Glue, a Teqequipment Net (NJ) Fluke pressure transducer module and multi-meter, a Ningbo Changqui Fluorine Plastic Products Co., Ltd.'s, (China) CFPC thread seal tape, itronix Inc. (CA) rounded tip stainless steel probes, and VWR Labshop, (IL) tygon plastic tubing (Figure 21, Figure 22, Figure 23, Figure 24, Figure 25, Figure 26, Figure 27).

Figure 21: KCD IP LLC. (IL) Craftsman air compressor.

Figure 22: Watts (MA) hex nipple and pipe tee.

Figure 23: Gorilla Glue Company's (OH) Gorilla Glue.

Figure 24: Teqequipment Net (NJ) Fluke pressure transducer module and multi-meter.

Figure 25: Ningbo Changqui Fluorine Plastic Products Co., Ltd.'s, (China) CFPC thread seal tape.

Figure 26: Itronix Inc. (CA) rounded tip stainless steel probes.

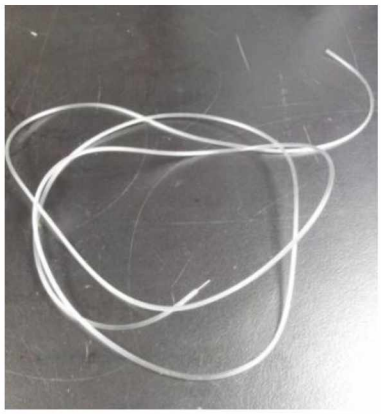

Figure 27: VWR Labshop, (IL) Tygon plastic tubing.

3.3 Determining the Optimal Plasma Oxygenation Bonding Procedure

Both the SR-3000 layer and the PDMS substrate are first treated at the same time by plasma in the reactor shown in Figure 17, and then brought in contact for bonding. The plasma treatment is controlled by three parameters; the radio frequency (RF) power, plasma treatment time, and the pressure in the reactor. For this study, 144 samples were prepared alternating the three control parameters. The number of 144 was calculated for eight different time lengths, two different vacuum levels, and three different power levels; and each combination was repeated for three times. Each sample is constituted with a SR-3000 piece and a PDMS substrate. For each of these samples the testing was conducted at ambient temperature by using unfiltered air as the process gas in the plasma chamber. In the following portion of the paper, the sample preparation procedures are first introduced, followed by and explication of the testing procedures.

In the first step 1”x1” PDMS substrates are prepared. Each PDMS substrate was prepared by mixing the PDMS elastomer (Sylgard 184, Dow Corning) with its cross-linking agent at the 10:1 ratio (by weight). The PDMS samples under the bonding strength test were created from the same blend and container so as to limit the chance of variability in the mixture. The PDMS is then poured into the mold shown in Figure 28, which is a 1”x1”x2” aluminum container 0.17” deep (5mm) with a 3mm diameter and 1mm height cylinder protruding from the middle to form the base of the pressure vessel.

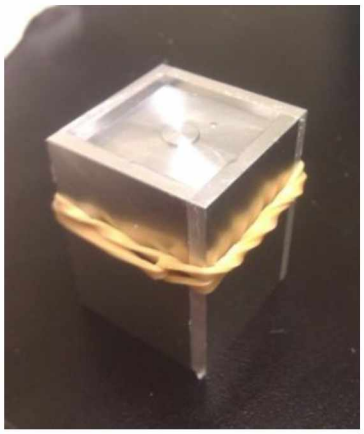

Figure 28: PDMS in aluminum pressure mold. At the center of the mold the protruded cylinder is to replicate the pressure chamber for testing the bonding strength.

The cylinder protruding from the aluminum is used to mold a chamber replica to serve as the pressure chamber for the pressure rupture testing. The dimensions of the sample were modeled in SolidWorks, which is shown in Figure 29.

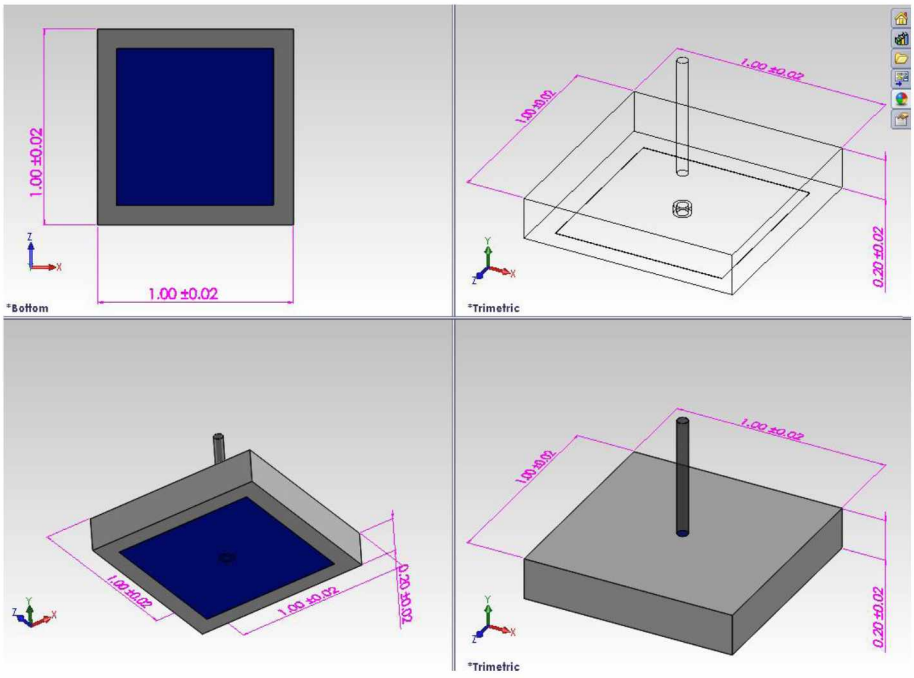

Figure 29: SolidWorks drawing of SR-3000 PDMS bonding test sample. (Dimensions in inches).

The aluminum molding was then placed in a vacuum desiccator (Figure 30), to remove all the air bubbles that formed during the mixing and pouring of the PDMS into the mold. The samples were run through the desiccator several times to ensure removal of any visible air bubbles.

Figure 30: Samples in vacuum desiccator for degassing and oven for curing.

The PDMS samples were then baked in an oven at 200° F for 20 minutes for curing (Figure 30). After curing the PDMS samples were removed from the oven and placed in ambient air for about 5 minutes to cool before peeling the PDMS from the mold. After the PDMS is pealed from the aluminum mold, a MHPM-UNV with a ϕ=0.023" diameter hole punch (Figure 31) was used to punch a hole through the PDMS in the round chamber. Next the PDMS was set aside in a Petri dish, covered, and waited for plasma treatment with the SR-3000 sheet as addressed in step 2 below.

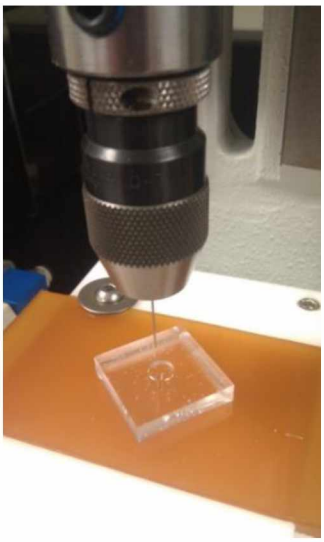

Figure 31: PDMS in hole press.

In the second step, the SR-3000 photoresist paper was cut into 3mm x 3mm squares and sprayed with warm water at around 45 psi over the rough side of the paper for 1 minute and 30 seconds (Figure 32). Wetting the SR-3000 sheet is to reproduce a wet condition as if the sheet had followed the conditions of channel fabrication in SR-3000 (cf. later in 5.3 Channel Design and Procedure).

Figure 32: 3mm x 3mm SR-3000 being washed with warm water for 1 minute and 30 seconds.

The PDMS (with the chamber side up) and SR-3000 (with rough side facing up) are then placed in the plasma reactor on a glass tray to undergo plasma treatment at an appropriate combination of the plasma control parameters. Once the plasma treatment was completed, the SR-3000 and PDMS samples were quickly removed from the plasma reactor (with tweezers), and then the treated surface of SR-3000 was placed on the treated surface of PDMS for contact bonding. At that time, pressure was gently applied to the bonded sample and then placed on a hot plate at 90° C for 2 hours. After this heat treatment, the sample was removed and was ready to be pressure tested.

Figure 33: Samples after testing and SolidsWorks close up of sample.

3.4 Rupture Test Procedure

The rupture test consisted of a compressed air injection system, whereby compressed air was guided into the chamber of each specimen (Figure 33). The pressure was increased slowly until the bond between the SR-3000 and PDMS was ruptured. The Craftsman air compressor was used to produce the needed compressed air pressure for the testing. The detail of experiments is addressed below.

The compressed air was guided in series to a pressure sensor (Fluke PV350, Tequipment.NET, Long Branch, NJ) and the pressure chamber through a pipe tee (Watts A-370, 0.25 in FIP), as shown in Figure 22. A 0.025" OD metal tube (New England Small Tube, NH) was press fitted into the access hole of the specimen (which is 0.023" in diameter) and then using a 0.02-in ID plastic Tygon tubing (63018-044, VWR Labshop, Batavia, IL) to interconnect the metal tubing and the pipe tee. The pressure sensor converts the measured pressure into voltage that can be read out by a multimeter (Fluke 83V, Tequipment.NET, Long Branch, NJ) on which the sensor is mounted. The specimen was placed in a cup of water so that any rupture or gas leakage could be evident by observing bubbles in the water (Figure 34).

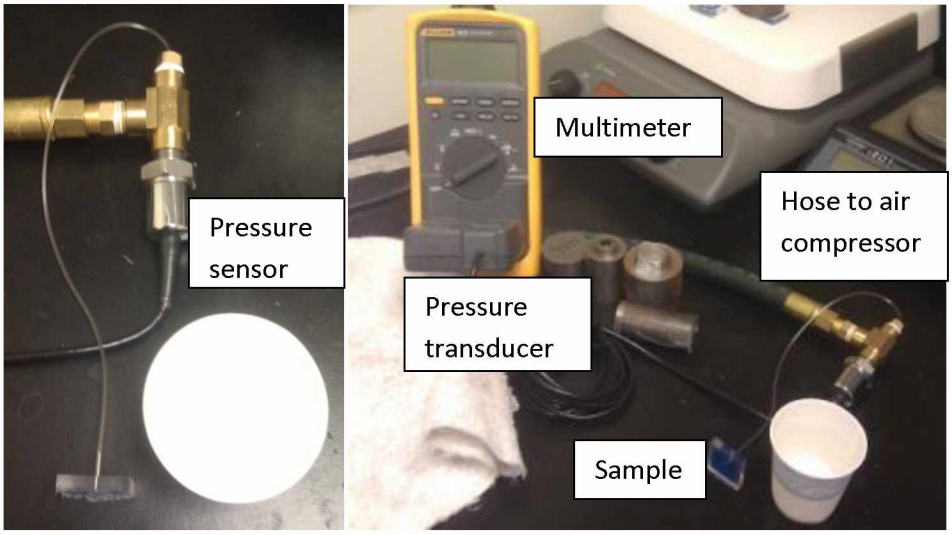

Figure 34: Set up prior to pressure rupture test.

For each sample under rupture pressure testing, the pressure in the chamber was first raised to 10 psi, and then was increased at a rate of 1 psi for every 10 seconds. The sample was also monitored during the process so that, once bonds began to break, the pressure remained constant to allow for the ripping between the two surfaces to stop. The sample was placed in water for visual detection of the moment when rupturing occurs. The pressure was always increased until the bond ruptured as seen in Figure 35.

Figure 35: A sample just ruptured in the rupture testing.

3.5 Results and Discussions

The rupture pressure listed in the table was the average of three test results. The bonding strength was measured for different plasma treatment parameters: the exposure time, chamber pressure, and the power at which the plasma is generated. The test results are summarized in Figure 36 and Figure 37. The results are also summarized in **Error! Reference source not found.** in Appendix.

From the data gathered the minimum bonding strength was found to be no lower than 19.7 psi, while the overall bonding strength average was found to be 29.6 psi. The maximum bond strength of 55.0 psi, was found at a combination of plasma treatment parameters of 200 mTorr and 18 Watts for 40 seconds in plasma treatment of the bonding surfaces. From this result it can be determined that the strongest bond strength occurs when conducting plasma treatment in 200 mTorr and high power setting (18 W) for 30~40 seconds or in 300 mTorr and low power setting (6.8W) for 20~30 seconds. The information provided in Figure 36 and Figure 37 can also serve as a "recipe" for bonding, as one can adopt any plasma treatment parameters from there to predict the bonding strength.

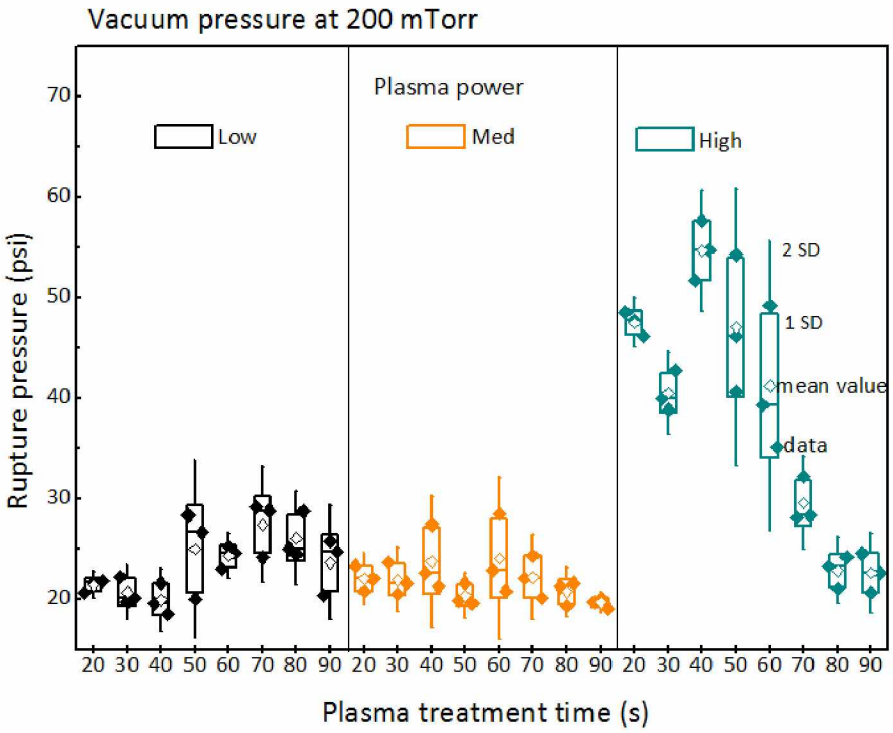

Figure 36: 200 mTorr rupture pressure test data graphically varying different plasma treatment parameters of treatment time and power.

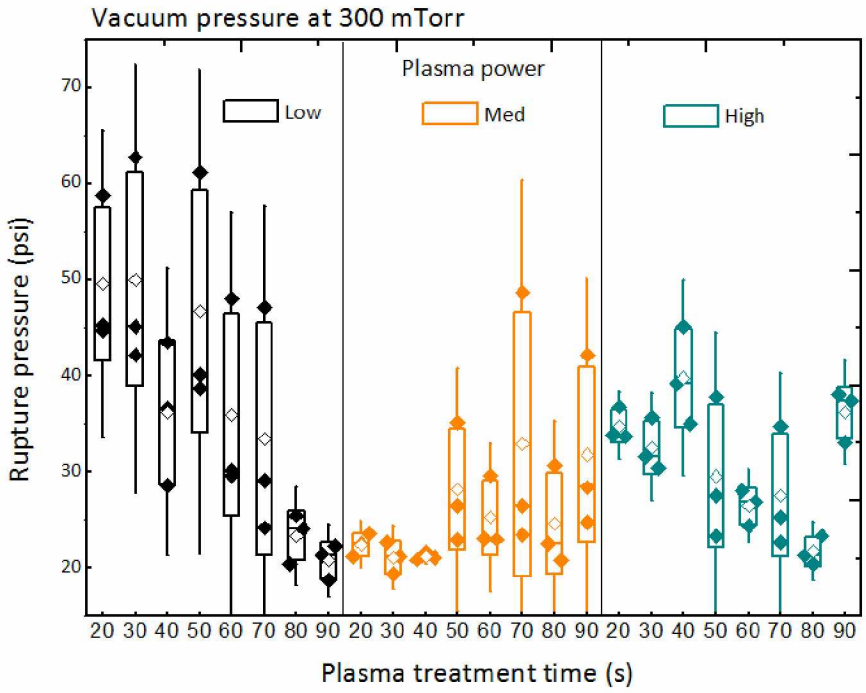

Figure 37: 300 mTorr rupture pressure test data graphically varying different plasma treatment parameters of treatment time and power.

After completing all the rupture tests for the bonding between the SR-3000 and PDMS, an analysis of the failure of each SR-3000-PDMS assembly was conducted; some tested samples are shown in Figure 38. From this analysis it was found that there are three different modes of failure.

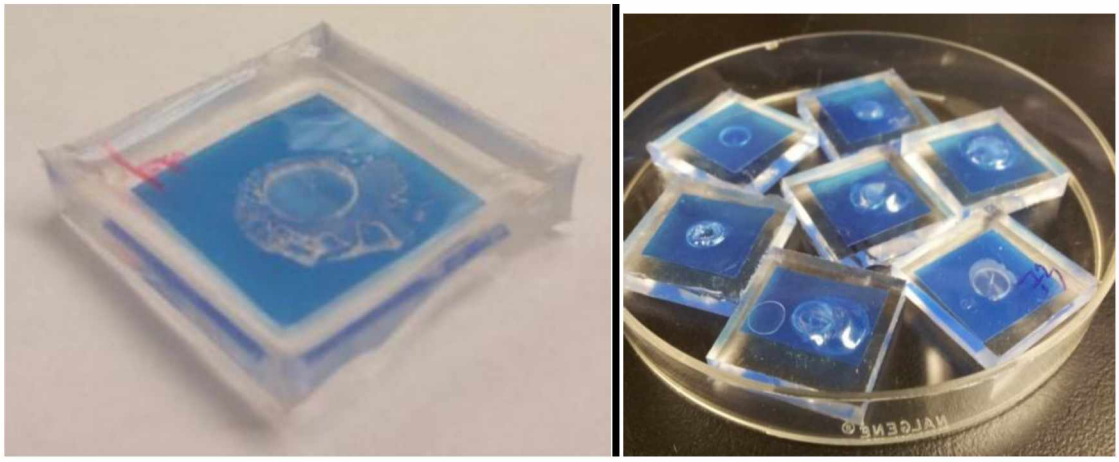

Figure 38: Samples after rupture pressure test.

The first mode of failure is a rupture between the bonded SR-3000 and PDMS (Figure 39), which is the most popular among the samples tested. In this failure mode the rupture occurs at the rim of the pressure chamber, and then gradually propagated outward, while the pressure chamber is intact.

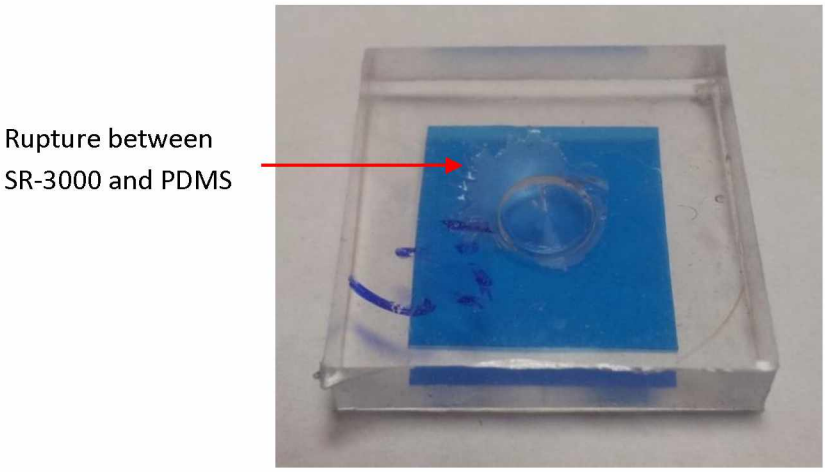

Figure 39: First mode of failure between SR-3000 and PDMS bond.

The broken pressure chamber, after the rupture pressure testing, is the second mode of failure (Figure 40). In this failure mode the PDMS piece remains intact and the pressured air ruptures the SR-3000 film (which is 5 mm thick). This mode is the least common among the samples tested.

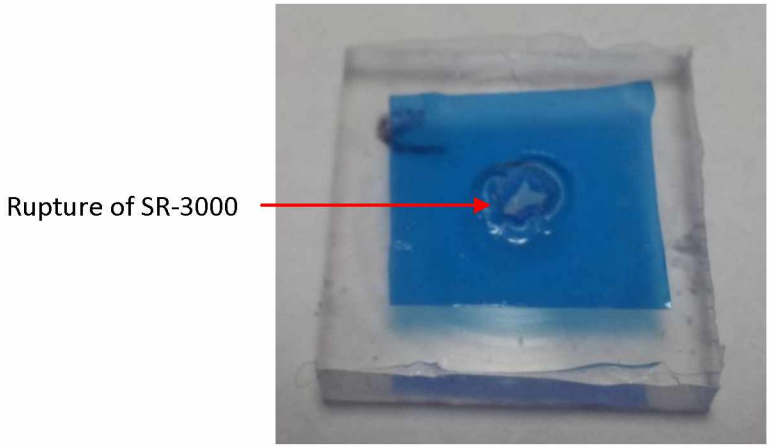

Figure 40: Second mode of failure between SR-3000 and PDMS bond.

The third mode of failure is a combination of the first and second modes of failure (Figure 41). In this failure mode, damage was observed at both the SR-3000 and PDMS interface and the pressure chamber. Under the rupture testing, pressurized air is gradually introduced to the pressure chamber and the SR-3000 film gradually expands, causing the bond between the SR-3000 and PDMS to break from the rim of the chamber.

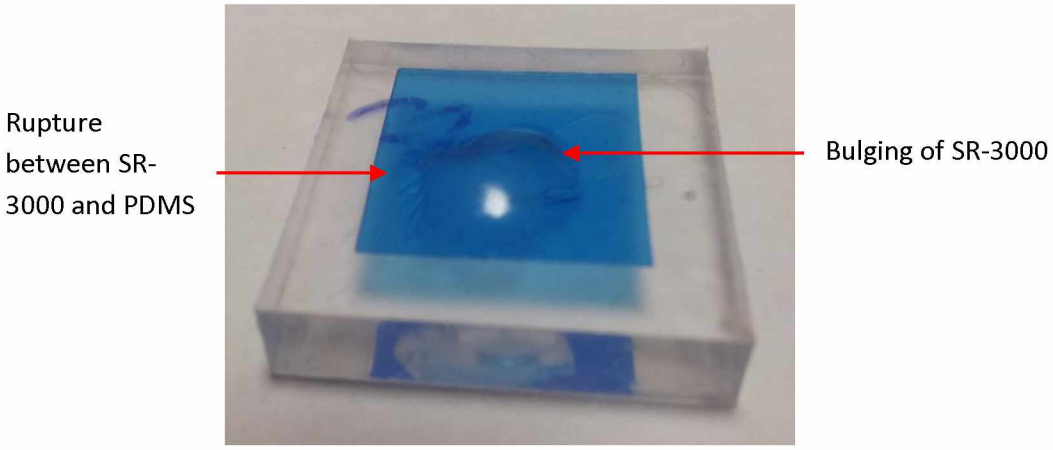

Figure 41: Third mode of failure between SR-3000 and PDMS bond.

3.6 Conclusion

The rupture pressure testing was conducted by slowly introducing pressurized air into a chamber, which was fabricated in the PDMS side and then sealed by bonding a SR-3000 photoresist paper to the PDMS. The bonding was made possible by first plasma-treating the surface of the PDMS and the SR-3000 photoresist, and then bringing the treated surfaces in conformal contact for bonding. The plasma was produced in the plasma reactor by adjusting three control parameters: the plasma exposure time, chamber pressure, and the power at which the plasma is produced. Collectively, 48 different combinations of the plasma treatment parameters were tested in order to find the best bonding parameters. Three SR-3000-PDMS assembly samples were prepared for each combination of the plasma treatment parameters. Therefore, a total of 144 samples were prepared by bonding the SR-3000 photoresist paper to the PDMS substrate to test the bonding strength created through unfiltered air plasma bonding.

The maximum averaged bonding strength measured is 55 psi, which was in a sample bonded by using 200 mTorr and 18 Watts for 40 seconds for plasma treatment of the bonding surfaces. It shows that the best bonding can be reached by conducting plasma in 200 mTorr and high power setting (18 W) for 30~40 seconds or in 300 mTorr and low power setting (6.8W) for 20~30 seconds. The test results show that the bonding strength is sufficient to hold the pressure for many microfluidics applications.

The results show that an integrated microfluidic module can be made by bonding SR-3000 to PDMS. The bonding test conducted in this chapter is critical, as it proves the feasibility of bonding PDMS to SR-3000 for prototyping microfluidic channels.

Chapter 4 Hydrophilicity of Plasma Oxygenated SR-3000

4.1 Introduction

The hydrophilicity of a surface has a profound implication on the operation of fluids in microfluidics. For example, the bonding strength of PDMS-PDMS can be correlated to the contact angle of water on the oxidized PDMS surfaces (Baszkin, Nishino, TerMinassian-Saraga et al., 1976; Tsuchida and Osawa, 1994; Murakami et al,. 1998; Bhattacharya, Datta, Berg, & Gangopadhyay, 2005). Determining the hydrophilicity of a channel surface is also important to the production and control of droplets (Baroud, Gallaire, & Dangla, 2010).

One way to characterize the hydrophilicity is to place a deionized water droplet on the surface of interest and measure its contact angle. In a study performed by Haubert et al. 2006 a BD2-AC hand-held corona treater was used to modify the chemical properties of the PDMS surface and then the contact angle of a water droplet on the treated surface was measured. This study showed that the contact angle for a droplet of deionized water is 92° on an untreated PDMS surface, while the angle is 105° on the treated surface. This study concluded that the contact angle could be an indicator of the extent of plasma exposure on the PDMS surface. In this chapter the goal is to characterize the hydrophilicity of the SR-3000 photoresist paper by measuring the contact angle of a deionized water droplet on plasma-treated SR-3000 surface.

Figure 42 illustrates the set up, which was used to measure the contact angle of the droplet on the SR-3000.

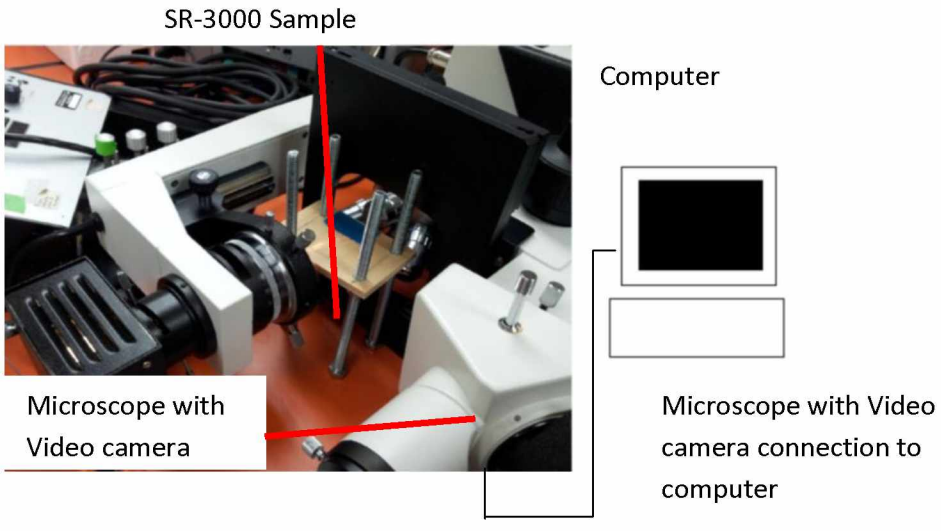

Figure 42: Contact angle measurement system set up.

4.2 Equipment Used to Determine Contact Angle

The goal of this section is to measure the contact angle of a deionized water droplet on a treated SR-3000 surface which is exposed to a variety of plasma treatment parameters. The control parameters include the plasma exposure time, the plasma power, and the vacuum pressure at which the plasma is conducted. Those parameters are selected from the 48 combinations aforementioned in Chapter 3, in order to find any correlation between the contact angle (to be measured) and the bonding strength reported in Chapter 3.

As mentioned in Chapter 3, the SR-3000 photoresist paper was purchased from Rayzist Photomask INC. (Vista, CA). The equipment needed for this testing included a Harrick Plasma (NY) Plasmaflow PDC-FMG and Plasma Cleaner PDC-32G, an Oerlikon Corp. (Switzerland) Trivac D2,5E vacuum pump, and a Samsung Galaxy S2 Stop Watch (South Korea) plate. (Refer to Figure 6, Figure 17, Figure 18, Figure 19, Figure 20 for these equipment and devices.)

Each sample was handled with TDI International Tweezers 2A-SADH (Switzerland) to reduce any particle contamination of the SR-300 surface. Droplets were introduced to the sample surface by using a 10mL HSW syringe (America). An Accu-Scope 3030 Microscope series (NY) (objective of PL4/0.01 160/-) equipped with a Photron Fastcam PCI R2 (CA) was used to take the droplet image on a computer screen to measure the contact angle. An equivalent magnification of 40x coupled with a 10x eyepiece magnification to view the contact angle was used. The contact angle was measured with a Roting Architectural Protractor (Germany, Figure 43, Figure 44, Figure 45, Figure 46, Figure 47).

Figure 43: TDI International Tweezers 2A-SADH (Switzerland).

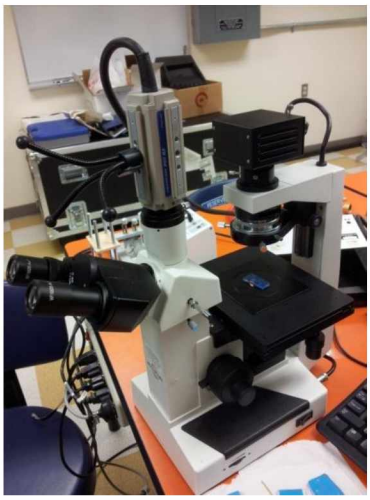

Figure 44: Accu-Scope 3030 Microscope series (NY).

Figure 45: 10mL HSW syringe (America).

Figure 46: Photron Fastcam PCI R2 (CA).

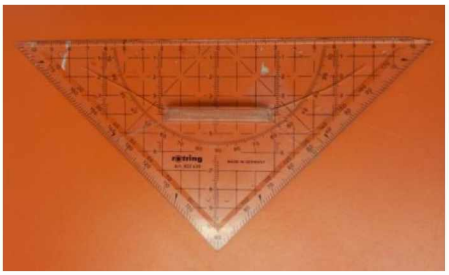

Figure 47: Roting Architectural Protractor (Germany).

4.3 Test Set-up and Contact Angle Measurement Procedure

The test samples were cut from the 3-mil SR-3000 into square 1cm x 1cm pieces. The sample size and shape were cut to allow for the contact angle to be tested three times on each specimen, as shown in Figure 48.

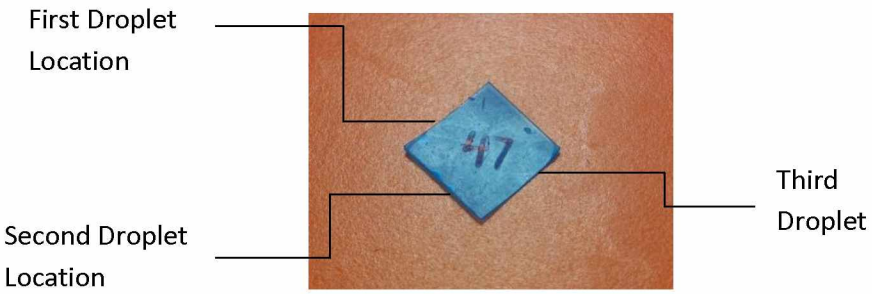

Figure 48: Sample #47 with noted droplet placements.

Each sample was then placed inside the plasma reactor, individually, and exposed under different exposure settings, by varying time, intensity and pressure (Figure 49).

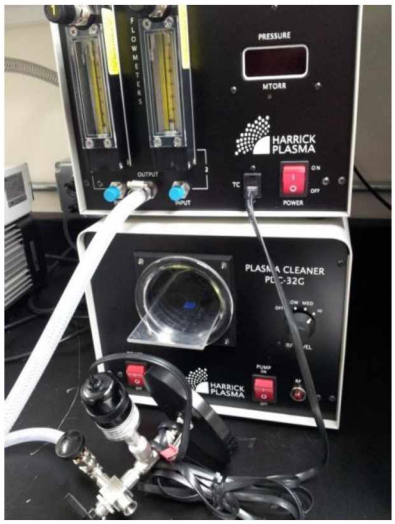

Figure 49: Sample placed in plasma chamber.

After the exposure in the plasma reactor, each sample was removed and numbered for identification. The sample was then placed in a 50mL beaker containing deionized water for storage prior to performing the contact angle test. This would allow the exposed sample to maintain a state of hydrophilicity longer, similar to in PDMS after its plasma exposure, however, the long-term stability of the oxidized surface on the SR-3000 is unknown (Duffy et al., 1998). Once it is time to measure the contact angle a numbered piece was taken out of the deionized water and allowed time for the surface to dry from being exposed to the ambient air. After it

was dried, a sample was placed on the mounting table in the Microscope (Figure 50) one at a time. A corner of the sample was viewed using the Fastcam camera (which is mounted on the microscope) after adjusting the mounting table. Once the sample was positioned properly in the microscope viewing area, a deionized water droplet was then place onto one corner of the sample using a syringe (Figure 51). Immediately after placing a droplet on the SR-3000 surface a photo of the droplet was taken to view the contact angle (Figure 52). The droplet was prepared with a 10mL HMS syringe as seen in Figure 45, so that each droplet has a volume between $5.0x10^{-6}$ m^3 to $7.0x10^{-6}$ m^3. Each droplet image was taken by a screen snap-shot.

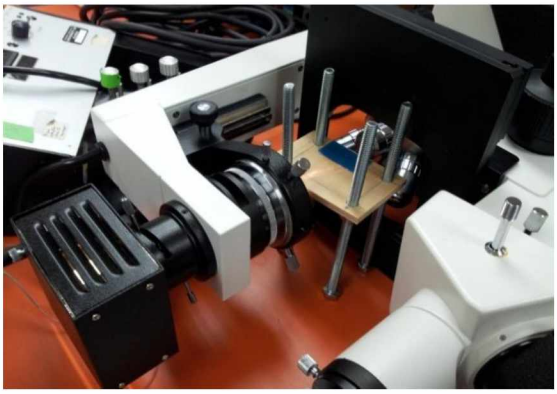

Figure 50: Sample in the microscope.

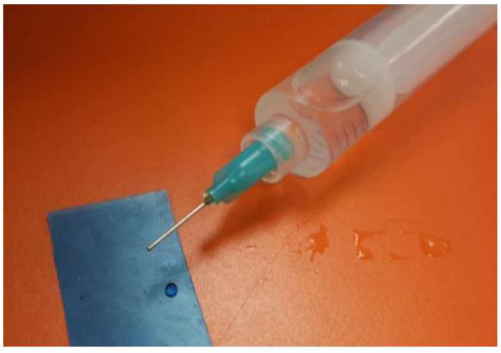

Figure 51: Droplet produced by syringe.

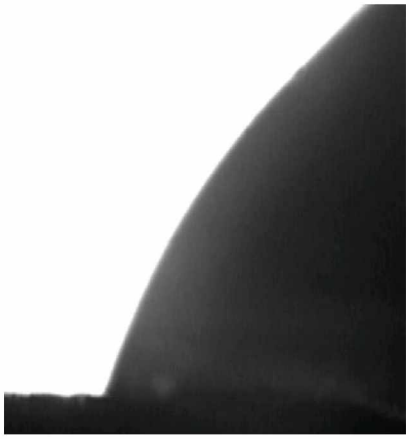

Figure 52: Close up view through microscope focused on contact angle.

The images of each droplet sitting on a SR-3000 sample were taken every 30 seconds for 5 minutes. The 5-minute measurement duration was determined as follows. After running several test runs on a non-exposed piece of SR-3000, we found that at the 5 minute mark the deionized water droplet will be absorbed into the SR-3000 sheet. The procedure as mentioned in Chapter 4 above is repeated two more times to measure the contact angle of droplets at the other two corners, as shown in Figure 48.

After completing three, 5-minute contact angle measurements, the contact angle was measured with a protractor on the droplet in each droplet image taken (Figure 53). Due to the fact that on each sample three droplets were placed, an averaged contact angle was obtained by the three measurements on each sample. To ensure consistency among the contact angle measurements, each angle was measured at room temperature.

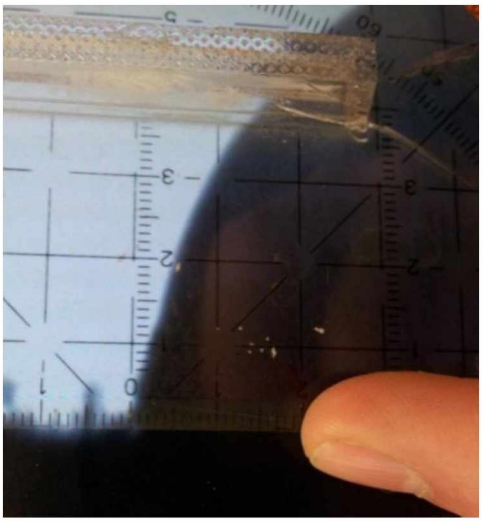

Figure 53: Protractor measuring contact angle.

4.4 Results and Discussions

The contact angle was observed over a 5-minute period to monitor the change in the droplet contact angle until it grew too small to be determined from the surface of the SR-3000. Figure 54 shows the typical evolution of a deionized water droplet on the plasma treatment of SR-3000 surface. Given such a short observation duration it is believed that the droplet's depletion was not due to evaporation, leaving the only explanation to be that a portion of the droplet was absorbed into the SR-3000 sheet.

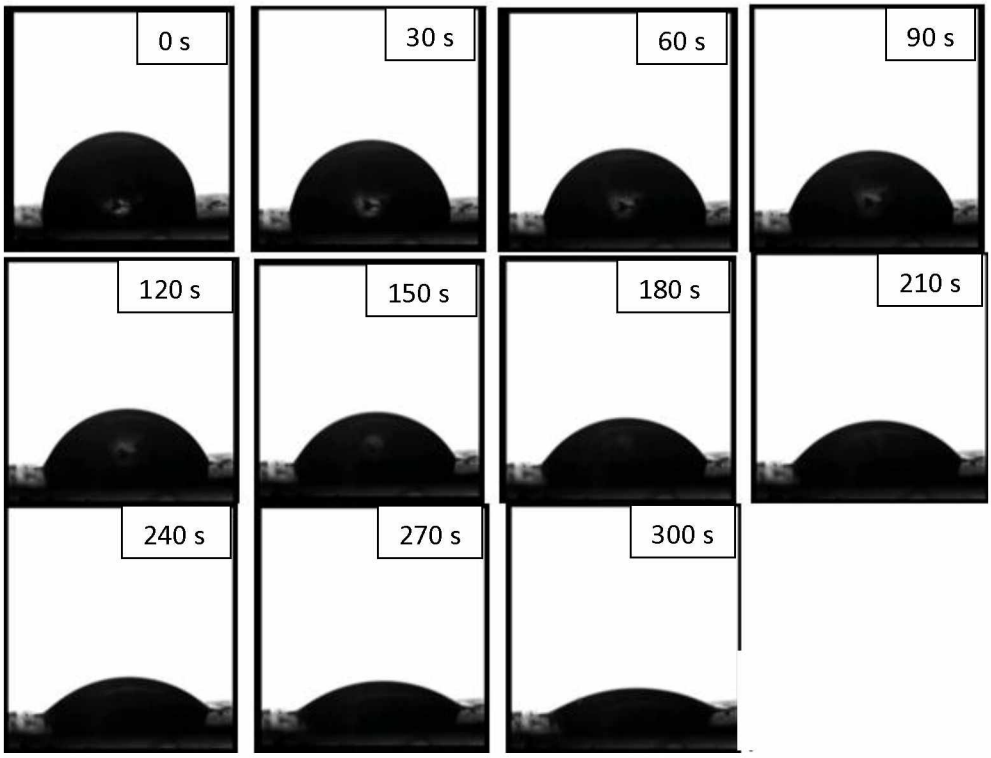

Figure 54: Sample #14 Droplet Change From 0-5 Minutes. Pressure=207 mTorr, Power= 18 W, and Treatment Time= 40 seconds.

The contact angle displays some interesting effects on the surface of SR-3000 that had been exposed to plasma. Below in

Table 2 and Table 3 are the measured data for the droplet contact angle (the data for these two tables is compiled in Table 6 of Appendix 7).

Table 1: Contact angle measured right when the droplet was placed on the SR-3000 surface which was plasma treated by the corresponding parameters.

	Exposure Time (s)								
AVG. Contact Angle (psi)	Vacuum Pressure (mtorr)	20	30	40	50	60	70	80	90
	200	80.73	87.43	92.23	94.07	94.77	92.20	87.33	82.60
	300	65.93	75.47	86.90	89.20	89.30	87.33	78.50	72.97
POWER	200	82.80	82.80	84.07	88.67	94.37	93.77	91.23	87.27
LOW	300	60.73	63.00	76.60	82.00	89.50	102.20	97.90	92.23
MEDIUM	200	72.43	75.40	76.77	81.20	78.00	70.57	63.17	57.53
HIGH	300	56.23	62.03	66.03	79.60	88.57	87.37	76.17	70.33

Table 2: Contact angle measured 30 seconds after the droplet was placed on the SR-3000 surface which was plasma treated by the corresponding parameters. (The data in Table 1 and Table 2 are compiled into Table 7 in the Appendix).

	Exposure Time (s)								
AVG. Contact Angle	Vacuum Pressure (mtorr)	20	30	40	50	60	70	80	90
	200	72.33	75.27	83.83	85.93	86.63	84.63	80.50	75.17
	300	63.53	75.03	80.60	84.80	83.23	85.20	83.07	73.07
POWER	200	76.97	74.77	75.73	80.27	85.53	84.33	83.00	80.23
LOW	300	58.17	59.50	73.43	76.83	80.63	91.37	90.87	85.83
MEDIUM	200	66.83	68.80	70.07	74.07	70.47	66.00	60.83	55.40
HIGH	300	53.60	60.03	63.67	75.07	81.70	79.73	74.07	65.97

From the data it was found that as the exposure time increased so did the contact angle between the two surfaces. This trend was held until around the 60-70 second mark, when any longer exposure caused smaller contact angles. The most interesting observation is that the phenomenon of the contact angle increasing and then later decreasing with longer exposure to

air plasma remains true regardless the pressures and power at which the plasma is generated. This means the additional parameters of pressure in the vacuum chamber during exposure and the power of the exposure do not have a large effect on the droplet's contact angle. This phenomenon can be seen more clearly by Figure 55, which is a graphical compilation of Table 1 and

Table 2.

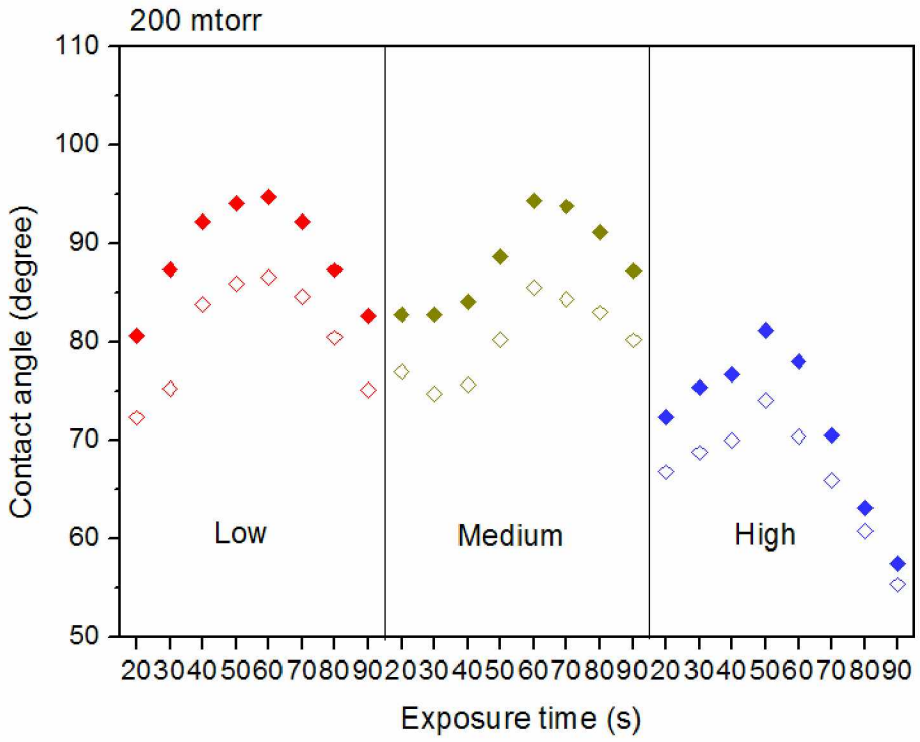

Figure 55: 200 mTorr Contact Angle Data Graphically. The filled in marks represents the contact angle at 0 seconds and the open mark is the contact angle at 30 seconds.

Figure 55 displays the data for the contact angle at a pressure of 200 mTorr while the exposure power and time are varied (Table 1 and

Table 2). From this figure it is can be seen that as the power of the exposure of the oxygenated plasma increases, the contact angle decreases. So for a lower power of exposure a larger contact angle can be achieved. Also from this figure the rate of change in contact angles over a 30 second time period can be seen as relatively constant for each droplet, meaning the pressure, exposure power and exposure time do not affect how quickly the contact angle will diminish over time.

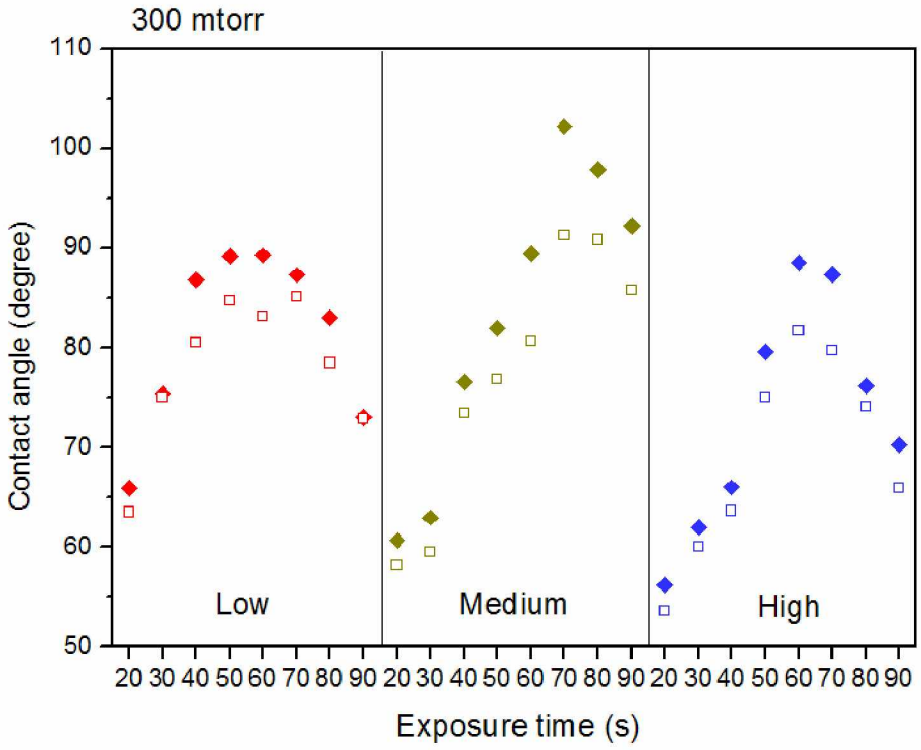

Figure 56: 300 mTorr Contact Angle Data Graphically. The filled in marks represents the contact angle at 0 seconds and the open mark is the contact angle at 30 seconds.

Figure 56 displays the data for the contact angle at a pressure of 300 mTorr while the exposure power and time are varied. One noted difference between the two graphs is that Figure 55 displays much less variation between the range of contact angle measured between the different power levels. Aside from that difference, both graphs share many of the sample trends in the data.

The maximum contact angle of 102.2°was achieved on a SR-3000 surface treated at a vacuum pressure of 300 mTorr, an exposure power of 10.5 W, and a time of exposure of 70 seconds. The

contact angle will play an important role in the interaction between the walls of the channel and the working fluid of the channel. A SR-3000 and PDMS microfluidic device would be unique compared to other microfluidic devices by having a channel formed with multiple materials. Since the fluid will interact differently with each material forming the channel, this could allow for additional characteristics and considerations when selecting a working fluid for the channel. While there is a difference between the contact angle of deionized water with SR-3000 and PDMS the discrepancy is not significant, and often within 2-3° of one another. This was confirmed by Haubert et al. 2006 in a study that observed the surface contact angle of PDMS after it had been treated by a BD2-AC hand-held corona treater. The study showed that the contact angle for a droplet of deionized water was originally at 92° and after treatment became 105°. It is important to note that the droplet interactions inside the channel will not largely vary between the contact with the SR-3000 and PDMS, allowing for an even distribution of friction on the droplet.

4.5 Conclusions

In this chapter the hydrophilicity of the SR-3000 photoresist paper was characterized by measuring the contact angle of deionized water droplets on a plasma-treated SR-3000 surface. It is well known that the contact angle on the plasma-treated PDMS surface is correlated to its bonding strength. This paper explored the hypothesis that the contact angle on the plasma-treated SR-3000 is also correlated to the plasma treatment parameters used in Chapter 3 of bonding strength characterization.

The important finding is that the contact angle of deionized water droplets on the plasma treated SR-3000 photoresist paper is a strong function of the plasma treatment time. While similar contact angles can be achieved by plasma exposed SR-3000 compared to PDMS, it is only true for some treatment times. For example, where the bonding strength between the two materials was strongest, the contact angle of deionized water and SR-3000 was only 76.8°. This is a much larger discrepancy between the contact angle of the fluid acting on the surface of PDMS and the surface of SR-3000. For data gathered, there was no clear correlation of the contact angle to the bonding strength. It will be important to consider how the contact angle and bonding strength could be correlated to one another, to ensure a high bonding strength can be achieved while forming a consistent channel wall interaction with the surface of the working fluid.

Chapter 5 SR-3000-PDMS Microfluidic Demonstrations

5.1 Introduction

This chapter demonstrates the feasibility of bonded SR-3000-PDMS modules to typical microfluidics applications. In the review conducted by Sia and Whitesides, 2003, it is pointed out that multiple fluid streams such as laminar flow and mixers are commonly exercised in biological studies, which is one major sector of microfluidics applications. Laminar flow allows for the predictable and controllable transportation of molecules or biological cells through microchannels for analysis. In chemical analysis and synthesis, this level of predictability and control is a key to simplifying the analysis and performing a controlled reaction (Takayama, 2003). On the other end, droplets can be used to platform many chemical and biological analyses, as the large surface-to-volume ratio enables rapid mixing and reaction in small droplets (The et al, 2008.). Here we apply the developed microfabrication method to prototype three microfluidic modules for operating laminar flow, achieving uniform mixing, and producing droplets, respectively.

It is worth mentioning that the goal of this chapter is to demonstrate the developed microfabrication method for its potential to broaden the perspective of microfluidics. Therefore, the goal of the demonstrations is twofold, prototyping a microfluidic module and making up one functional operation. As far as the discussion of the physical principles or parametric studies for each example, this paper will leave those issues for future work.

5.2 Equipment for Channel Fabrication

Among a variety of equipment for fabricating microfluidic modules made of SR-3000 and PDMS, the Mask Making Kit purchased from Rayzist (Vista, CA) plays a key role in developing microchannel patterns on the SR-3000 photoresist paper. The Mask Making Kit contained 15 sheets 8.5" x 14" of SR-3000, five UV Vellum sheets, Letralite exposure unit, hand sprayer with faucet adapter, a wash out board, and Magic Dark Toner Repair Kit (Figure 57, Figure 58, Figure 59, Figure 60, Figure 61, and Figure 62).

Figure 57: SR-3000 Rayzist Photomask (Rayzist Photomask INC., Vista CA).

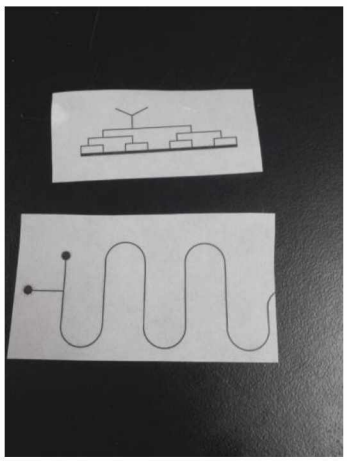

Figure 58: UV Vellum printed with channel patterns cut.

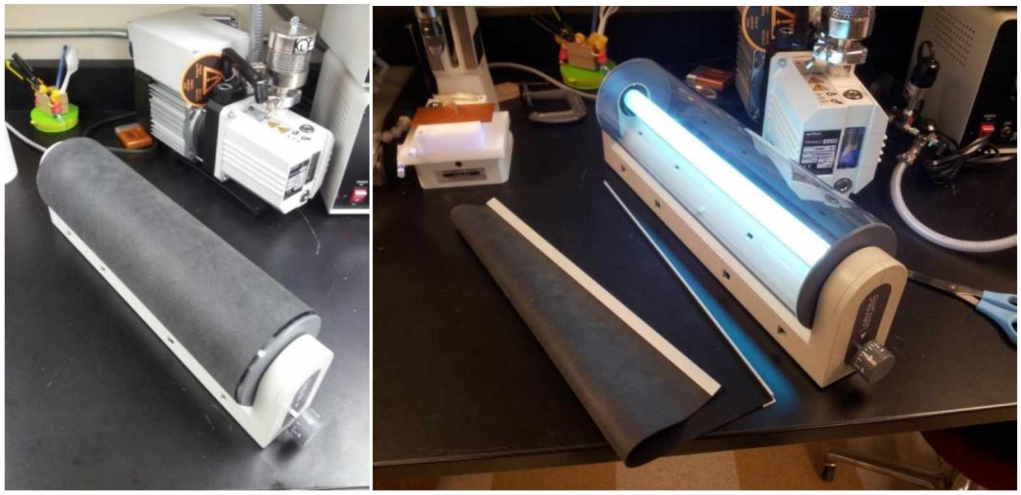

Figure 59: Ikonics Imaging Letralite black light (MN).

Figure 60: Spraying Systems Co. Trigger Jet Hand sprayer (150 max psi) (IL).

Figure 61: SR-3000 wash out board with magnetic strips.

Figure 62: Advance Chemical Engineering Acextra Magic Dark Spray (CA) with applicator.

Other equipment needed for fabricating microfluidic modules include a Harrick Plasma Plasmaflow PDC-FMG and Plasma Cleaner PDC-32G (Ithaca, NY), an Oerlikon Corp.(Switzerland) Trivac D25E vacuum pump, a Samsung Galaxy S2 Stop Watch (South Korea), a PC-620D hot plate (Corning, NY), and a laser printer with 1200dpi printing resolution (Figure 17, Figure 18, Figure 19, and Figure 20).

5.3 Channel Design and Procedure

The photoresist vender Rayzist provides a few options of the photoresist papers. Among them, the SR-3000 is 3 mm thick and best fits our need of fabricating a microchannel a few hundred microns wide. The entire photoresist development process (which is also described as the "wash-out process" herein) is schematically overviewed in Figure 63.

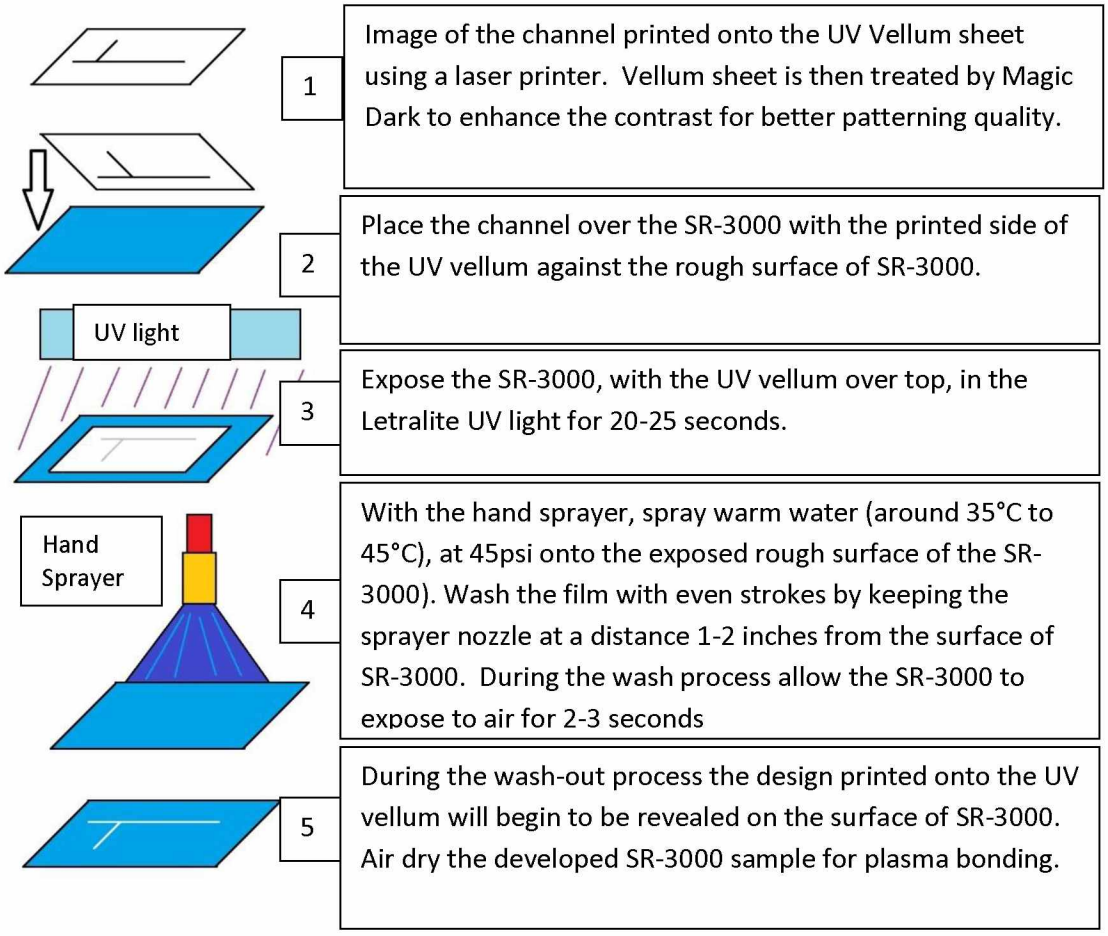

Figure 63: Schematic of SR-3000 channel wash out process.

In step 1, the channel design was first drawn in software such as Microsoft Word with a line width of 0.75pt. We then printed the drawing onto a UV Vellum sheet with a laser printer (Figure 64). The Vellum sheet was purchased from Rayzist (Vista, CA). A printer with a 1200 dpi resolution was used to ensure the UV vellum sheet would have the maximum amount of ink to

block any incoming light from the Letralite black light. A printer with higher resolution would provide better printing quality on the Vellum sheet.

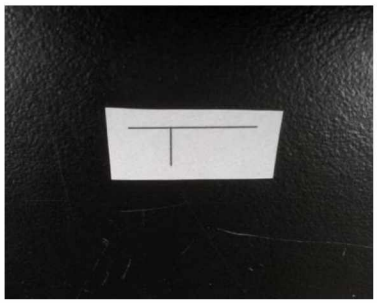

Figure 64: Channel pattern printed onto UV Vellum at 1200 dpi.

The UV vellum sheet was then treated with Advance Chemical Engineering Acextra Magic Dark Spray, which helped create more intensive contrast on the image printed on the Vellum sheet to render the printed pattern darker and the un-patterned region lighter. After the UV vellum was treated with Magic Dark, it was allowed to air dry for 15 minutes to ensure that the chemicals have set in the UV vellum sheet. Figure 65 compares the contrast between the printed patterns on the Vellum sheet (A) before and (B) after applying the Magic Dark Spray.

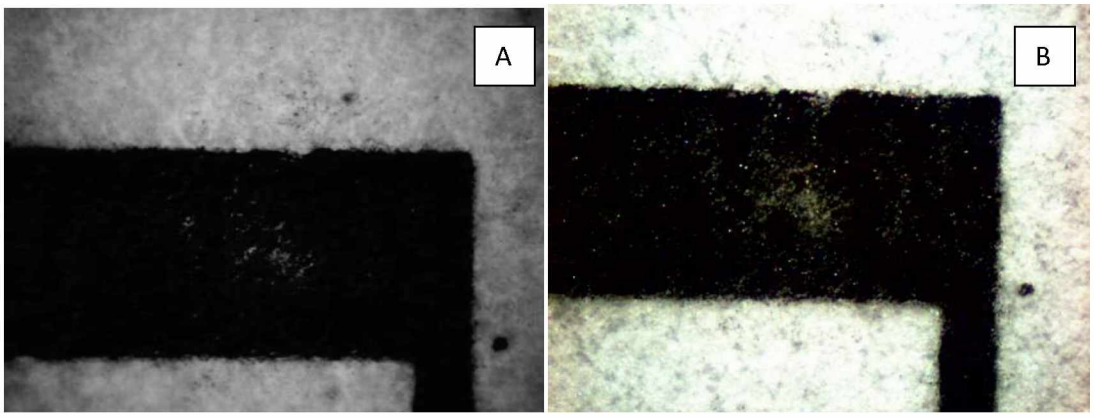

Figure 65: Comparison of a patterned printed on vellum sheet. A. Printed channel without the application of Magic Dark. B. Printed channel with an application of Magic Dark.

The finished Vellum sheet (printed, sprayed, and dried) served as a stencil mask to transfer the pattern (e.g., microchannels) printed on the sheet to the SR-3000 photoresist paper for further development.

In step 2, the vellum stencil mask (on which the channel pattern was printed and treated with Magic Dark) was cut out of the finished Vellum sheet (with scissors). In addition, a piece of SR-3000 photoresist paper was cut into a size, which is about 0.25" larger than the Vellum stencil at each side (Figure 66). This extra space was required for securing the SR-3000 sheet during the development process.

In the third step of the fabrication process in Figure 63, we placed the Vellum stencil mask against the rough side of the SR-3000 film (with the printed side of the stencil mask in a conformal contact to the SR-3000) (Figure 66). Manual alignment may be needed to ensure a good overlay of the two sheets, while leaving a 0.25" space along the perimeter of the SR-3000 film. Then we placed the overlaid sheets on the Letralite black light (Figure 67). From the work conducted in the lab, the best results were found when the stacked UV vellum film and SR-3000 are placed in the Letralite unit directly above the black light, after which we turned on the power of the Letralite and exposed the SR-3000 film for about 20-25 seconds. The timing for the exposure was important, as under or over-exposure will be detrimental to the pattern development (e.g., non-uniform pattern development our of a uniform pattern image).

Figure 66: SR-3000 film rough matte side up underneath the Letralite black light with the printed side of the UV vellum against the rough side of the SR-3000.

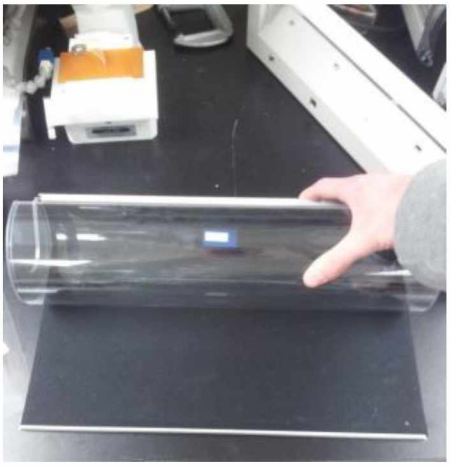

Figure 67: SR-3000 and channel pattern being wrapped in the Letralite blanket before being placed over the black light.

Step 4 was intended to develop the pattern by washing-out the unexposed region in the SR-3000 film with warm water. The SR-3000 film was secured with the exposed rough blue matte side up, to the metal washout board with magnetic strips as seen in Figure 68. The hand sprayer was connected to a faucet (Figure 60) with warm water (between 35°C to 45°C) and with the nozzle at around 1-2 inches above the SR-3000 surface. Then the film was washed with even and slow strokes, slowly backing away as the channels begin to wash out as not to over wash the channel from the surface (Figure 69).

Figure 68: SR-3000 sheet prepared for washout.

Figure 69: Hand sprayer at the appropriate distance from the SR-3000 film during wash out.

It is worth mentioning that for such compact channel designs, the SR-3000 paper during the washout process requires some exposure to air. Continuous exposure of the SR-3000 film to water seemed to cause undesirable washouts of the photoresist and lead to varied channel widths, which could also be a result of under- or over-exposure under UV light in Step 3. Therefore, intermittent water spay to the SR-3000 film will help develop a smooth and uniform pattern after the washout process. This was accounted for by repeating the cycle of spraying the SR-3000 for 5 seconds, then stopping for 2 seconds.

In step 5 of Figure 63, the image is more visible during the washout process because the photoresist in the unexposed channel region is gradually washed away. The design pattern on the SR-3000 film is shortly revealed (Figure 70). The total washout times ranges from one to 2 minutes.

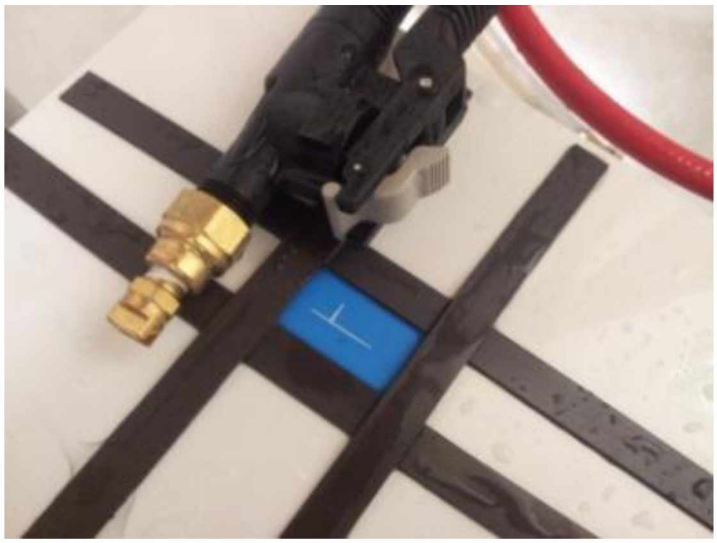

Figure 70: SR-3000 after successful channel washes out.

After the washout is completed, the SR-3000 photoresist sheet needs to dry before the plasma bonding can take place. The wet SR-3000 sheet was found to take around 15 minutes to dry when exposing the film to ambient air conditions. The drying process may be shortened by using a hair dryer at a low temperature setting. Once the surface of the SR-3000 film is dry, it is ready to be plasma bonded to PDMS. The process used to plasma bond SR-3000 and PDMS was detailed earlier in chapter 3.

5.4 Characterization of Microchannels in SR-3000

When introducing a new method to produce a microchannel. It is important to analyze the walls of the microchannel. To do this, channels of varied width were prepared in SR-3000 to examine their profile. The channel profile was measured using both a scanning electron microscope (SEM) and conventional desktop microscopes. The SEM has many advantages over traditional microscopes. The SEM has a large depth of field, which allows more of the specimen to be in focus at one time compared to that of a standard microscope. The SEM also has a much higher resolution, so closely spaced specimens can be magnified at much higher levels. A SEM uses electromagnets rather than lenses; the researcher has much more control in the degree of magnification. All of these advantages, as well as the actual strikingly clear images, allows for more accurate images and measurement of the channel profile (Figure 71).

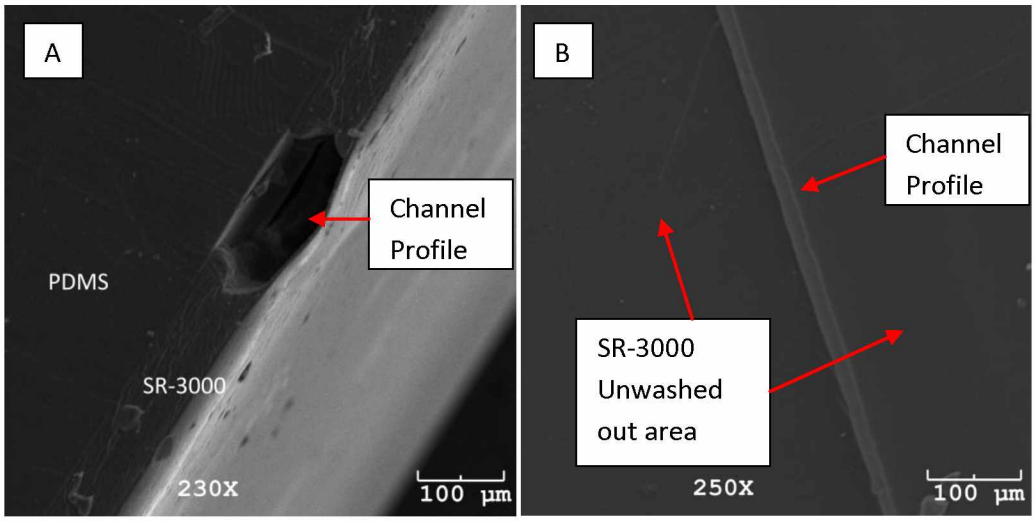

Figure 71: SEM produced channel profile. A: The cross-section. B: Run-through.

Image A in Figure 71 shows the cross-section of a microchannel made out of the SR-3000 photoresist paper and sealed by PDMS. In the image, the channel formed in the SR-3000 washout process can be clearly seen. Note that as the un-exposed material in the channel region was washed out, it left an un-washable layer in the SR-3000. This un-washable layer is thin and flexible. This is an important finding, as the flexibility of the layer may allow channels created in SR-3000 to expand like a valve, to actually reduce. From the limited testing conducted, the amount of which this flexible layer can displace is based on the pressure of the working fluid in the channel. Image B in Figure 71, is a top view picture of the channel profile.

To more clearly see the creation of channels in SR-3000, a Digital Blue QX5 Computer Microscope (Atlanta, GA) was used to take colored images of the channel (Figure 72).

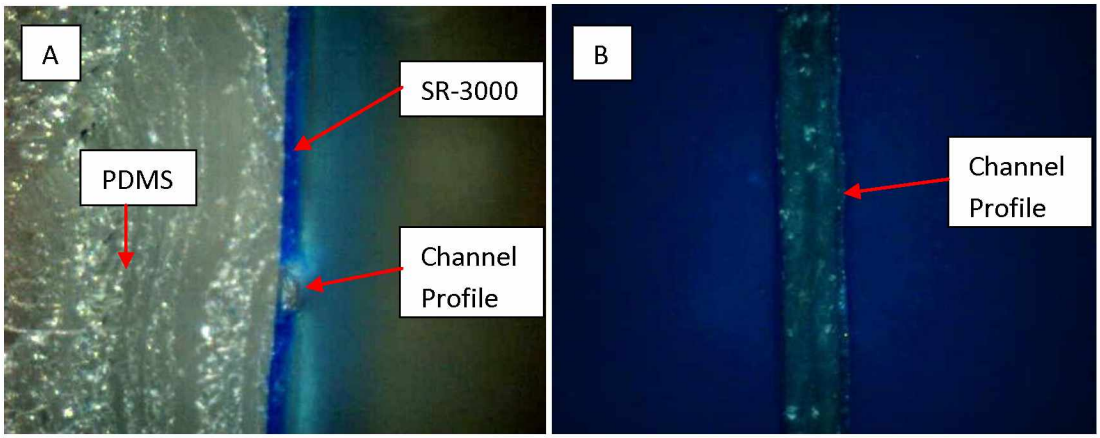

Figure 72: Traditional microscope produced channel profile at 60x. A: Cross-sectional view. B: Run-through view.

Image A in Figure 72 shows the cross sectional profile of the channel in SR-3000 that has been bonded to PDMS. In the image the channel being formed from the SR-3000 washout process can be seen as labeled. Image B, in Figure 72 is a top view of the channel profile. This image provides a better view of the roughness of the side walls of the channel. It shows that the microchannel produced out of the SR-3000 has a smoother profile than that of the channel made by the Shrinky-Dink process (Bender, 2011).

To further compare the channel profiles, images were taken of a SR-3000 PDMS and a Shrinky-Dink microchannel at similar magnifications. These additional images were taken of the channel profile with increased zoom on the same channel section, before working fluids were run through the channel (Figure 73, Figure 74, Figure 75, Figure 76). These images were the best representation for the smoothness of the side walls of the channel, compared to a Shrinky-Dink channel, Figure 73, the first image in the comparison between the two channel fabrication methods. At this magnification there appears to be little difference between the wall roughnesses of the two channels. However, along the center of the channel the SR-3000 has a much smoother channel wall (labeled in figure).

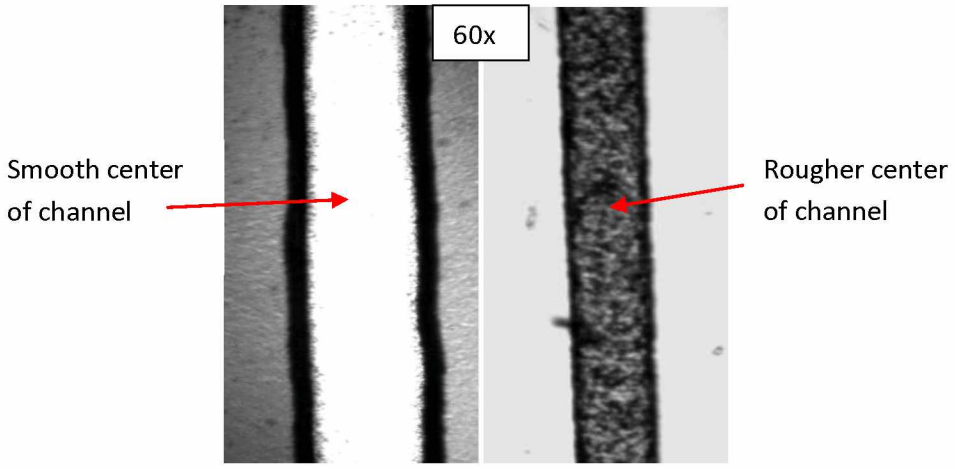

Figure 73: Top down view of channel walls at 60x zoom. Left: SR-3000 PDMS Microchannel. Right: PDMS-PDMS Microchannel.

Figure 74 compares the different channel fabrication types at 120x. At this higher magnification the SR-3000 PDMS channel has a much smoother wall profile along the channel. Additionally, the smoothness of the center of the channel can be more clearly seen. The channel was also measured using the measuring tool onboard the microscope to find the difference in channel width.

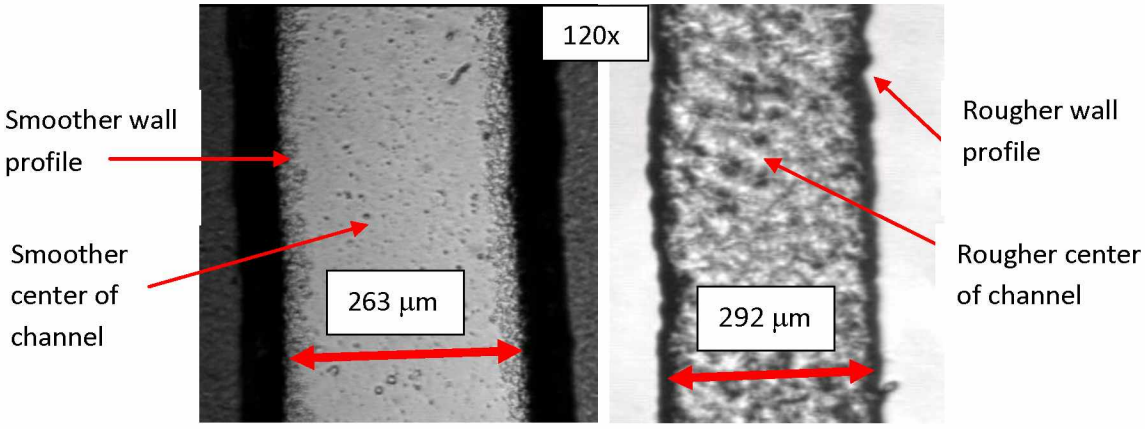

Figure 74: Top down view of channel walls at 120x zoom. Left: SR-3000 PDMS Microchannel. Right: PDMS-PDMS Microchannel.

Figure 75 is where the difference in roughness between the two channel types can be most clearly seen. Roughness along the channel walls will have large impacts on the fluid flow in the channel and on the droplets. Rough channel walls will create inconsistencies between droplets produced in the channel, as well as increase undesired drag forces acting on the droplets, which can negatively influence their velocity and contact angle.

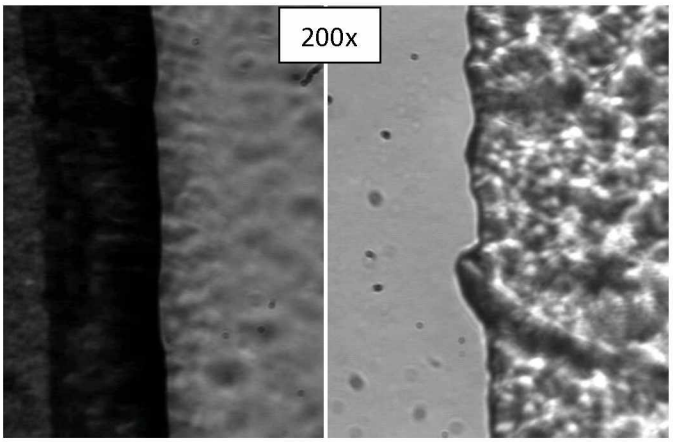

Figure 75: Top down view of channel walls at 200x zoom. Left: SR-3000 PDMS Microchannel. Right: PDMS-PDMS Microchannel.

Figure 76 compares the channel profiles at 400x magnification. At this magnification roughness along both channels can been seen. However, larger more impactful inconsistencies can be seen in the Shrinky-Dink channel.

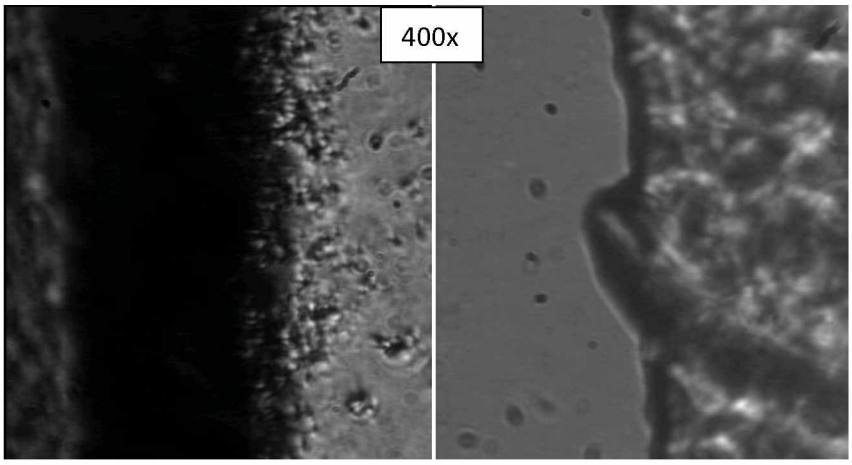

Figure 76: Top down view of channel walls at 400x zoom. Left: SR-3000 PDMS Microchannel. Right: PDMS-PDMS Microchannel.

5.5 Prototyping Designs for Demonstrations

Three different designs have been prototyped to demonstrate the applications of the microfluidic modules made of integrated SR-3000 photoresist paper and PDMS to typical microfluidic operations: laminar flow, mixing of different fluids, and droplet production.

5.5.1 Demonstration of Laminar Flow

The first is the "Dog Bone" design, which features two Y-junctions that meet at a 45° angle (Figure 77). A stream of oil and water will be respectively injected at each of the Y branch. The two immiscible streams will meet at the Y junction and then continue flow down the length L_1. This design is used to demonstrate the laminar flow in a microchannel made out of the SR-3000 photoresist paper and sealed by PDMS. The dimensions in the Figure 77 are determined arbitrarily to allow for easy viewing with a microscope.

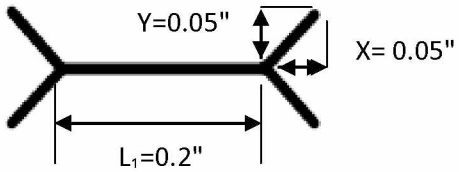

Figure 77: Dog bone channel design to demonstrate laminar fluid flow. 0.75pt line width.

Flow is defined as either laminar or turbulent based on the dimensionless Reynolds number, which is defined as (Bringer, Gerdts, Song, Tice, & Ismagilov, 2004):

$$Re = \frac{\rho V L}{\mu}$$

Equation 1: Reynolds Number.

Where:
ρ is the density of the working fluid
V is the mean velocity of the fluid
L is the width of the microchannel, and
μ is the dynamic viscosity of the fluid

Any flow with the Reynolds number smaller than 2000 is defined as the laminar flow, which is typical for flows in microchannels. In chemical analysis and synthesis, laminar fluid control is important because it is both streamlined and predictable, further simplifying the analysis (Takayama, 2009). Due to the channel size fabricated (shown shortly in Figure 71), it is predicted that an insignificant extent of diffusive mixing will occur along the length L_1.

The evaluation of laminar flow in the channel was conducted by running water and oil into the channel. Laminar flow was visually confirmed by observing the flows down the stream without mixing. Figure 78 shows the Y-junction where water and oil flows first meet. At their initial interaction it can be seen that the interface between the flows are parallel to the flow direction, an evidence of laminar flow. The fluid flow rates for this demonstration are documented in Table 3.

Table 3: Fluid flow rates for laminar flow.

Test Title	Working Fluids	Flow Rate	Reynolds number
Y- Junction Flow	Oil	18.9 uL/min	1.936x10^-10
	H2O	18.9 uL/min	6.524x10^-8
Farther Down Channel Flow	Oil	18.9 uL/min	1.936x10^-10
	H2O	87.5 uL/min	3.021x10^-7

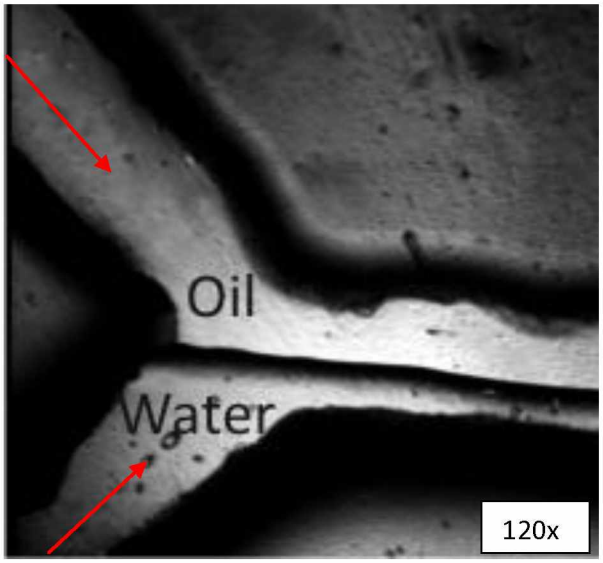

Figure 78: Oil and water flows meet at the Y-junction of channel (at 120x magnification).

To confirm that the flows in the channel are laminar, the interaction of the water and oil was observed through the entire channel down the stream. The images in Figure 79 were taken at the mid section of the dog bone design, further away from the first Y-junction. When at first trying to evaluate the fluid flow in the mid section of the dog bone channel, it was detected that the oil flow dominated the channel due to the similar flow rates of the two fluids. To get clearer separation between the water and oil flows, the flow rate of water was increased in an effort to create the boundary between the flows in the middle of the channel. The flow rates for both the Y-junction and mid channel flow are noted in Figure 79.

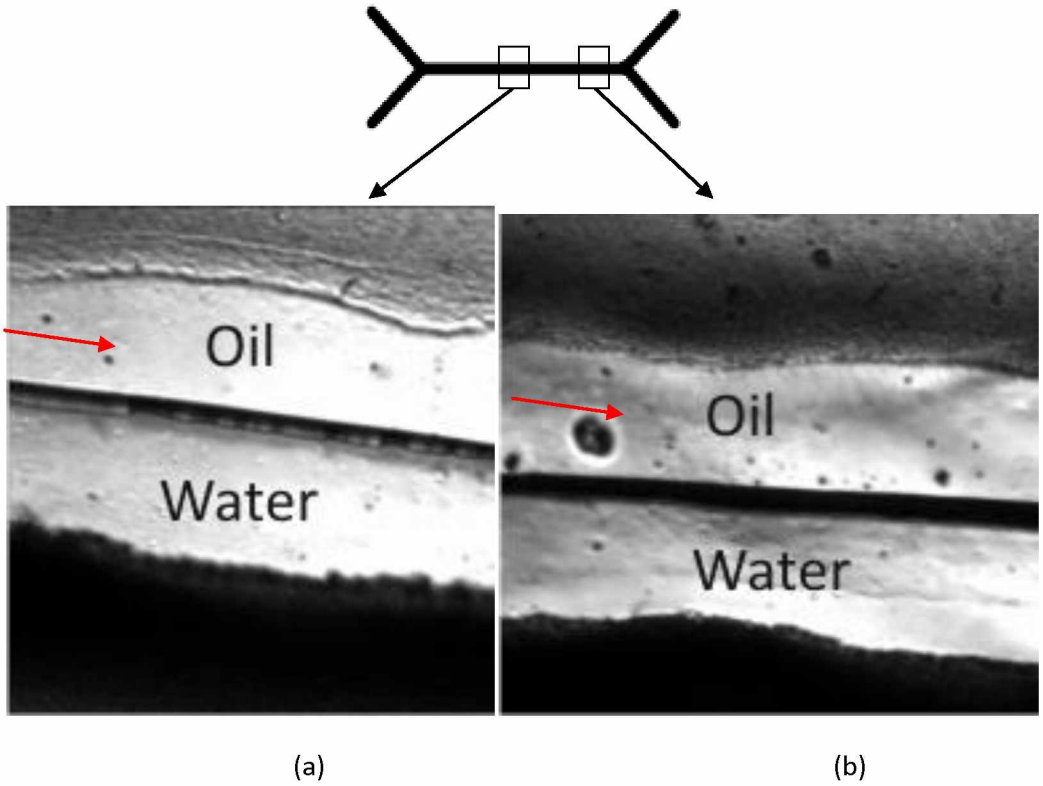

Figure 79: Oil and water laminar fluid flow in channel at 60x magnification. (a) Fluid flow 5cm from the Y-junction. (b) Fluid flow 10 cm from the Y-junction.

5.5.2 Demonstration of Water-Water Mixing

In microfluidics, mixing allows for two desired features of a system for making measurements of samples available in minute quantities: (i) rapid mixing of reagents, and (ii) low consumption of sample (Bringer et al., 2004). However, mixing in microchannels often imposes a challenge due to the low Reynolds numbers at which the fluid is operated. For laminar flow in microchannel, the mixing is often achieved by the so-called lateral diffusion, as schematically shown in Figure 80. Figure 80 illustrates the concept of lateral diffusion along the direction in the laminar flow of both the blue and red dyed water. This phenomenon is referred to as the Taylor's dispersion (Beard, 2001). The mixing is determined by the coefficient of diffusion of each dyed solution and the flow speed of the fluids. Usually a low Reynolds number and a large coefficient of diffusion facilitate mixing. This type of mixing often is conducted in serpentine channels and is determined by the flow rate and the coefficient of diffusion.

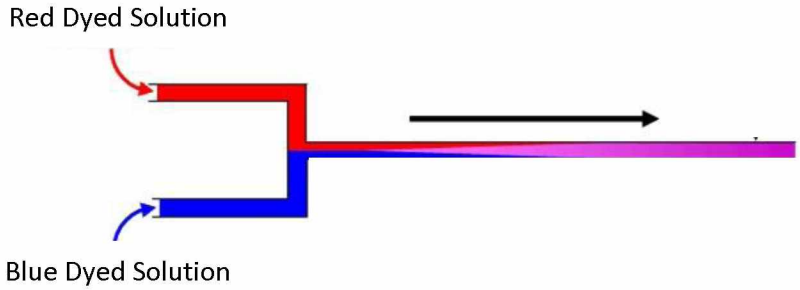

Figure 80: Diagram of diffusive mixing.

The second demonstration is the "mixing channel," which demonstrates mixing of two miscible fluids. We use two differently dyed aqueous solutions for demonstration. Water dyed in colors of blue and yellow was injected separately into the channel system through the Y branches (Figure 81). At the Y-Junction the fluids will meet and then begin to flow down through the channels. The two flows will finally meet at the bottom of the design, which contains a thick channel allowing the water to pool and display the mixed colors more clearly.

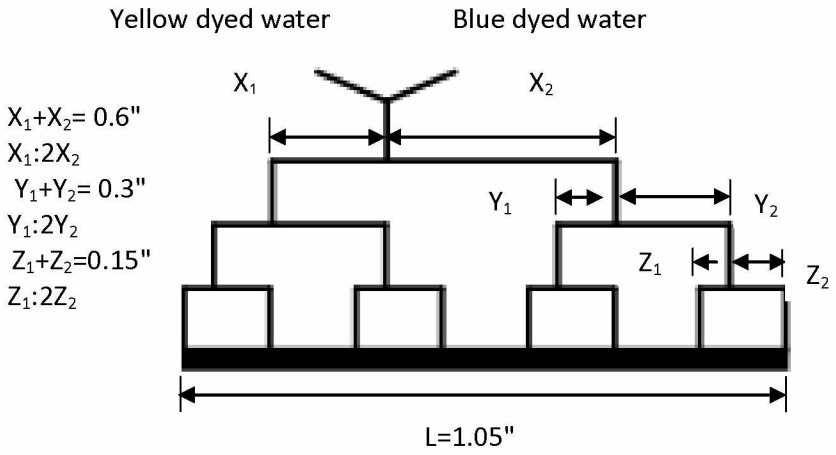

Figure 81: Mixing channel design. 0.75pt line width.

The assessment of mixing was done by observing a color gradient formed at the bottom channel of the design. Two dyed deionized water solutions were injected to the mixing channel, as shown in Figure 82.

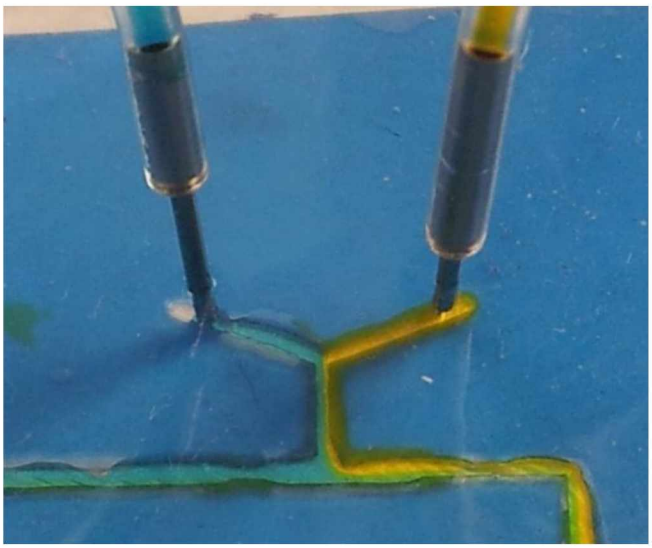

Figure 82: Blue and Yellow dyed water entering the Y-Junction displaying laminar flow.

Figure 83, clearly shows the mixing of the blue and yellow dyed water by the principle of Taylor's dispersion (Beard, 2001). We noted that a few air bubbles exist in the bottom-most chamber of this design, causing some "white spots." These bubbles disabled the flows from interacting, affecting their mixing through the channels. Attempts to remove the bubbles by guiding the bubbles toward the exit holes were unsuccessful. (Once an air bubble is formed in a microchannel, it is hard to remove because of the surface tension).

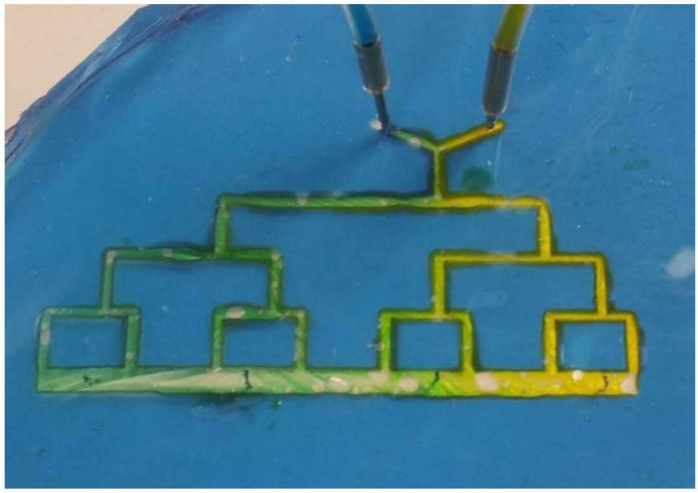

Figure 83: Mixing channel after 10 minutes of fluid flow, note the color pallet shifting from blue on left to green in middle to yellow on the right.

Table 4: Mixing channel fluid flow rates.

Test Title	Working Fluids	Flow Rate	Reynolds Number
Mixing Chamber Flow	Yellow Water	18.9 uL/min	6.524×10^{-8}
	Blue Water	18.9 uL/min	6.524×10^{-8}

5.5.3 Demonstration of Oil Droplet in Water Generation

The third design is the "T-Junction Channel," which is designed to produce droplets of oil in a stream of water flowing through the channel (Figure 84). When the two fluids meet at the T-junction it is expected that the water flow will shear the oil flow and produce oil droplets in the water flow.

Chemical and biological reagent has been show to be tied to droplet-based microfluidic systems as a form of monitoring their interactions. Due to the control and rapid mixing of fluids in a laminar flow channel the amount of time required to observe reaction times of chemical reagents in biomedical research has been reduced (The et al., 2008).

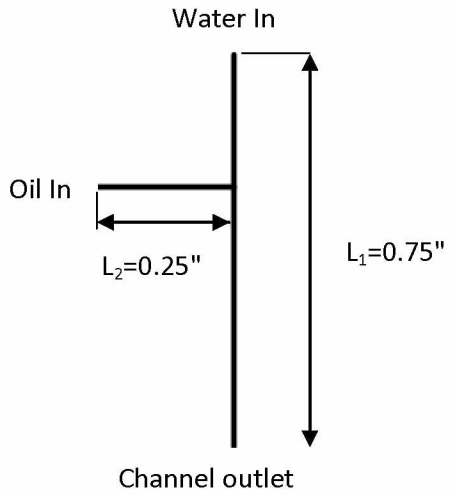

Figure 84: T-Junction Channel design to produce oil droplets in a water flow. 0.75pt width.

When producing droplets in a microfluidic channel, the interfacial tension and viscosity are the most important fluid properties to consider. For the droplets to form, it requires a shear force to separate the two working fluids. For this shear to occur the interfacial tension and viscosity compete with each other. A dimensionless number is used to quantify the relative strength of the two fluids, which is expressed by the Capillary number (Tice, Song, Lyon, & Ismagilov, 2003):

$$\mathrm{Ca} = \frac{\mu V}{\gamma}$$

Equation 2: Capillary Number.

Where:
V is the mean velocity of the fluid,
μ is the larger dynamic viscosity of the two working fluids, and
γ is the interfacial tension.

A low Ca number indicates that the stresses due to interfacial tension are stronger compared to the viscous stresses (Tice et al., 2003). A larger interfacial tension compared to the viscous stresses will force the droplets to minimize the surface area, which forms spherical ends on the droplet as it moves through the channel. Whereas a high value of Ca indicates that the viscous stresses will dominate the interfacial tension. This allows the droplets to become more deformable; the deformation of a droplet most often leads to the formation of a more asymmetric shape.

Channels with liquid-liquid interactions where the fluids have a different viscosity will cause the formation of droplets in the flow. Oil-in-water droplets is one of the most common ways to do this, with water having a constant stream flow with oil forming the droplets. The ability to form these droplets is determined by several factors such as viscosity of the fluids, the miscibility, the interfacial tension of the fluids, channel surface, and velocity, and can aid in the size and production rate of the droplets (Baroud et al., 2010). The droplets produced in the SR-3000 and PDMS channel were formed using a water miscible fluid, glycerol. Glycerol was added to reduce viscosity, thus increasing the dominance of the interfacial tension between the two fluids and allowing for easier shearing. Since this is a new method for fabricating microfluidic channels, different tests were conducted to form different types of droplets. The first type is where droplets have a diameter smaller than the width of the channel, and were successfully created as seen in Figure 85 and Figure 86. These droplets are a key in the production of different biological reagents. They also show that the channel is capable of transporting molecular particles or cells in the channel.

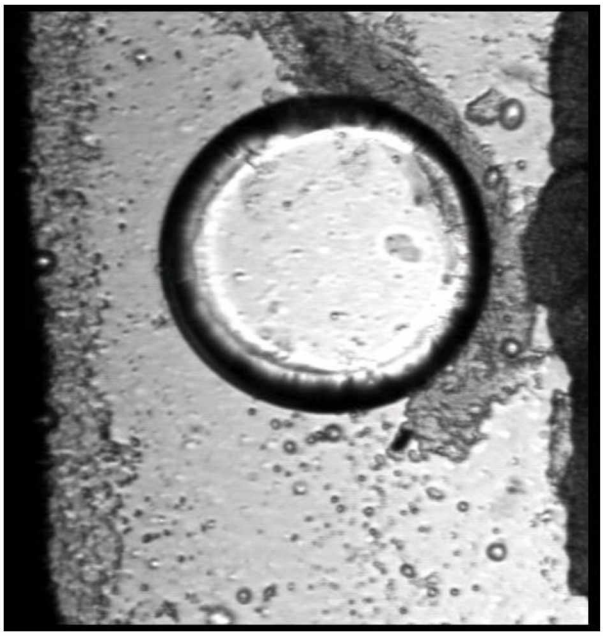

Figure 85: Oil droplet moving in a working fluid of water.

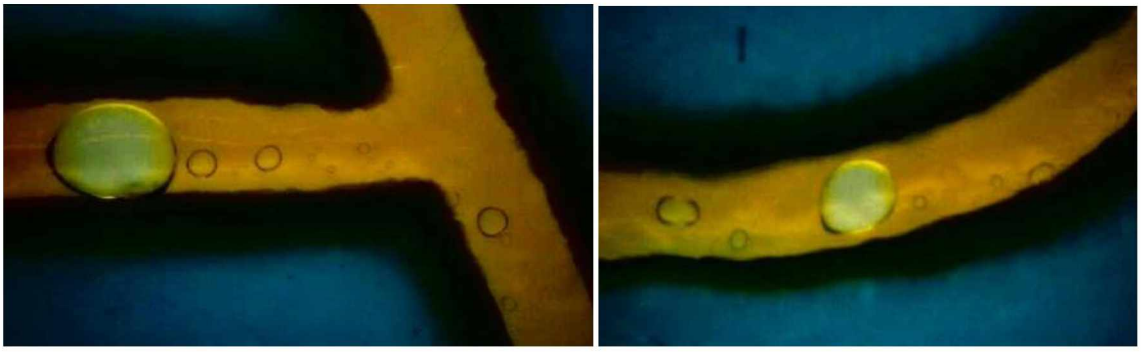

Figure 86: Oil droplets of varying size moving through a working fluid of dyed water.

The second type of droplet is the so-called "plugs," which are fully encased in the continuous phase fluid. The elimination of channel contact will prevent the plug from adsorbing to the channel, which can disrupt the reproducibility of the droplets. These droplets can be produced at various sizes. The plug motion is dictated by the channel dimensions as well as the flow rates of the water and oil streams at the T-junction. In Figure 87, the formation of the droplet plug is occurring as the oil flow interrupts the water stream. As the shearing to form the droplet occurs, soon a droplet will form. The droplet was then evaluated farther down the channel so it could be seen at a steady state condition as in Figure 88. The fluid flow rates for the droplet demonstrations are defined in Table 5.

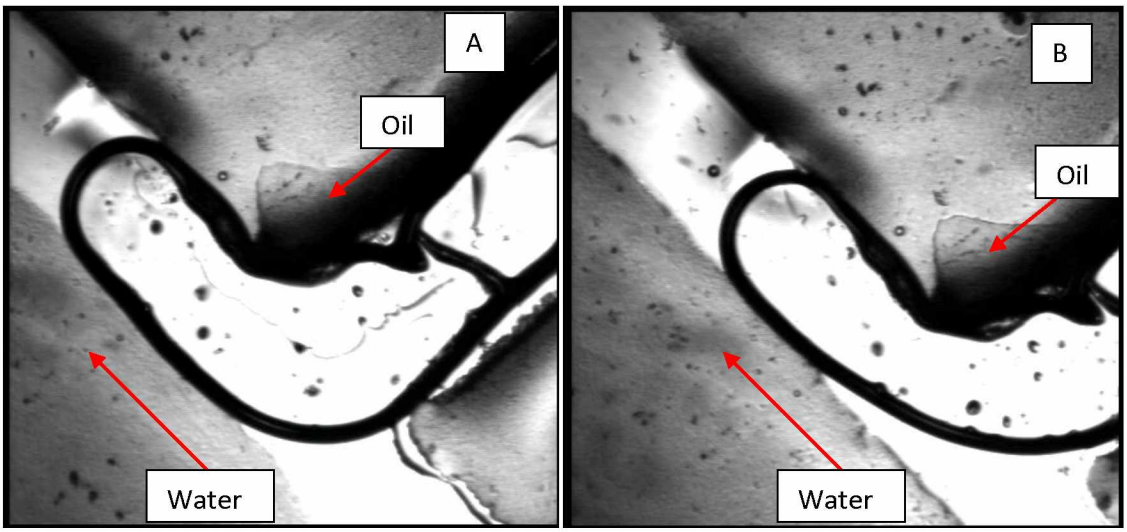

Figure 87: Beginning of the formation of a droplet plug of oil in water.

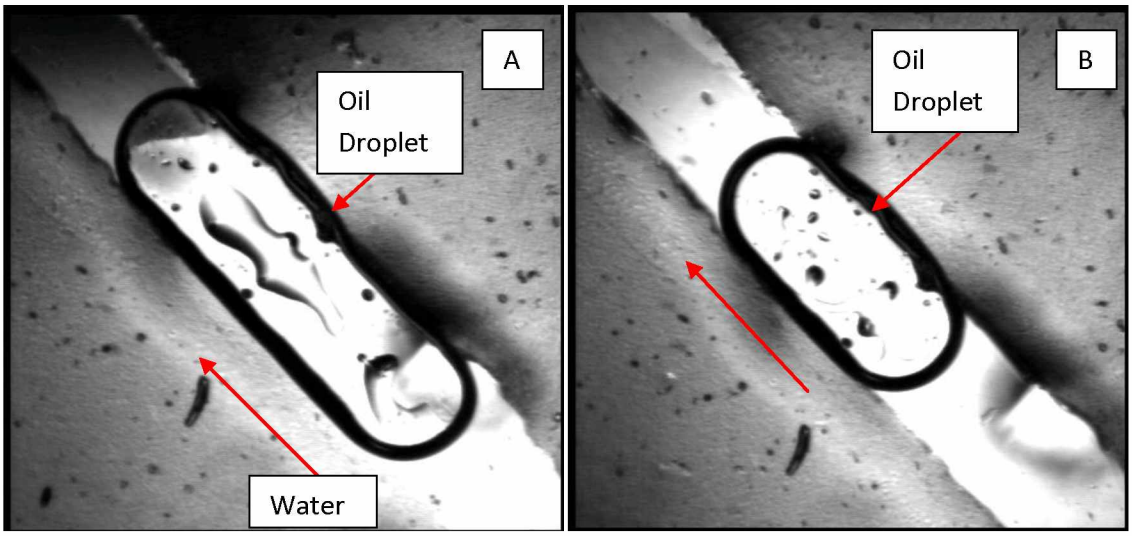

Figure 88: Droplet plug fully developed down channel.

Table 5: Droplet plug fluid flow rates.

Test Title	Working Fluids	Flow Rate	Reynolds Numbers
Droplet Production A	Oil	18.9 uL/min	$1.936x10^{-10}$
	H2O	18.9 uL/min	$6.524x10^{-8}$
Droplet Production B	Oil	18.9 uL/min	$1.936x10^{-10}$
	H2O	87.5 uL/min	$3.021x10^{-7}$

5.8 Conclusions

The Dog bone microfluidic device is a working demonstration of the SR-3000 and PDMS microchannels for operating laminar flow. Due to the small dimensions of the micro channel created in the SR-3000 the fluid flow was never able to reach a point of turbulence, which corresponds to a large Re number (~2000 or larger).

However, the channel roughness can influence the flow to create turbulent mixing of the working fluids (Koo & Kleinstreuer, 2003). The channel roughness has many other undesirable effects such as increased drag forces acting on the droplets causing reduced pressures, decreased velocities, and has fluctuating contact angles along the channel (Teh, Lin, Hung, & Lee, 2008). What can be concluded through the test performed on the Dog bone microfluidic

device is that the channel walls are sufficiently smooth as to not affect the flow from being laminar.

The diffusive mixing of two different color dyed water flows was demonstrated. While the formation of a color gradient in the bottom-most chamber of the mixing channel was achieved, it was somehow impeded by the formation of air bubbles there. The formed bubbles negatively affected the test by fogging the view of the color gradient, which was trying to be achieved. A more optimized design or a different fluid insertion method of the mixing channel should be considered for future work to display the diffusive mixing of the blue and yellow water flows. One suggestion being to first sweep the channels with a denser fluid then the intended working fluid to help remove any possible air. After removing the air then introduce the working fluid dyes to sweep out the denser fluid. This may ensure bleeding of both fluids out of the system while allowing all the air to be removed from the channel.

The last demonstration is to prototype a T-junction channel to produce droplets of various sizes. Droplets have a potential to become important tools for drug delivery and bio-sensing. In order for droplets to function properly, correct dosing and manufacturing must be ensured. While there was not an in depth analysis conducted on the consistency of the droplets produced by a T-junction in SR-3000, from the test performed, the ability to create droplets in a SR-3000 microfluidic device is possible. As with any microfluidic channel, the roughness along the channel was unavoidable. Additional studies should be performed comparing the roughness of SR-3000 and Shrinky Dink lithography as roughness can negatively affect the control of the fluids moving in the channel.

Chapter 6 Summary and Suggestions for Future Work

6.1 Summary

A new, rapid microfabrication method for prototyping microfluidic modules was presented in this thesis. In this method a commercially available photoresist SR-3000 was used as the structural material for creating microchannels and then bonded to PDMS, without access to the cleanroom facilities. It showed in Chapter 2 and 3 that SR-3000 is enriched of Si and its surface chemistry can be modified by plasma to form a strong bond to PDMS. The bonding strength was measured to be in the 20~60 psi range, depending on the parameters used in the plasma-assisted surface modification. The strongest bonding measured was achieved by using the following plasma parameters: a treatment time of 40 seconds, under 200 mTorr of pressure, and 18 Watts of power for plasma generation. One special feature in SR-3000 is that its surface becomes hydrophobic right after plasma treatment, yet the hydrophobicity quickly degraded in a few minutes, as depicted in Chapter 4. In Chapter 5, three different microfluidic modules were prototyped to demonstrate the feasibility of this new microfabrication method to typical microfluidic applications. The demonstrations include laminar flow control in microchannels, mixing, and droplet production. The success of each demonstration has not only proved the applicability of the integrated SR-3000-PDMS modules, but also introduced a new rapid and environment-friendly prototyping method to produce microfluidic channels at low costs.

6.2 Future Work

Additional research work is needed to better benchmark this new fabrication method:

- An Investigation into designing thinner channels and further testing the limitations of SR-3000 photoresist paper for developing microfluidic channels.
- Research on the ability of SR-3000 channels to flex as the pressure increases in the channels. The purpose is to study its potential as a pneumatic valve.
- Conduct more research on different geometry and more detailed patterns of the microfluidic channels in SR-3000.
- Continue research on how the contact angle of a droplet will vary on the surface of SR-3000 photo resist paper, after being exposed to plasma oxygenating bonding. Also testing on the droplet of different materials on the surface of SR-3000, such as glycerol.
- Study droplet control by varying channel width, design and the addition of surfactant to water. Surfactants should help to improve droplet uniformity and allow for more consistent results.

- Conducting research into the long-term use of SR-3000 in micro-fluid channels and how the material could degrade or change over a longer period. Due to SR-3000 property of absorbing liquid after long-term use, some of the working fluid in a channel is absorbed by the channel walls.
- Further investigation into the bonding strength of SR-3000 to PDMS and how to achieve higher bonding strengths, comparable with PDMS to PDMS bonding.
- Investigate how temperature treating SR-3000 will change the material properties during the microchannel fabrication process.
- Test the use of powder air mixture in a SR-3000 and PDMS channel.

References

Baroud, C. N., Gallaire, F., & Dangla, R. (2010). Dynamics of microfluidic droplets. *Lab on a Chip, Vol. 10*, 2032-2045.

Baszkin, A., Nishino, M., & Ter Minassian-Saraga, L. (1976). Solid-liquid adhesion of oxidized polyethylene films: Effect of temperature. *Journal Colloid and Interface Science, Vol. 54*, 317-328.

Beard, D. A. (2001). Taylor dispersion of a solute in a microfluidic channel. *Journal of Applied Physics, Vol.* 89, 4667.

Bender, C. (2011). Water-in-air droplet formation in plasma bonded microchannels fabricated by Shrinky-Dink lithography (Masters dissertation). University of Alaska Fairbanks, Fairbanks, AK.

Bhattacharya, S., Datta, A., Berg, J.M., & Gangopadhyay, S. (2005). Studies on surface wettability of poly(dimethyl) siloxane (PDMS) and glass under oxygen-plasma treatment and correlation with bond strength. *Journal Microelectromechanical systems, Vol.* 14, 590-597.

Bringer, M. R., Gerdts, C. J., Song, H., Tice, J. D., & Ismagilov, R. F. (2004). Microfluidic systems for chemical kinetics that rely on chaotic mixing in droplets. *Philosophical Transactions of The Royal Society, Vol. 362,* 1087-1104.

Dow Corning Corporation. (2011). *Sylgard 184 Silicone Elastomer Kit.* Retrieved December 22, 2011, from http://www.dowcorning.com/applications/search/products/Details.aspx?prod=01064291&type=PROD.

Duffy, D. , McDonald, J. C., Schueller, O. J. A., & Whitesides, G. M. (1998). Rapid Prototyping of Microfluidic Systems in Poly(dimethylsiloxane). *Analytical Chemistry, Vol.* 70, 4974-4984.

Harrick Plasma. (n.d.). *Plasma Products: Plasma Cleaners*. Retrieved February 13, 2012, from http://www.harrickplasma.com/products_cleaners.php.

Dittrich, P.S., & Manz, A. (2006).Lab-on-a-chip: microfluidics in drug discovery. *Nature Reviews Drug Discovery, Vol. 5*, 210-218.

Haubert, K. (2006). PDMS bonding by means of a portable, low-cost corona system. *Lab on a Chip, Vol. 6*, 1548-1549.

Hollahan, J. R., & Carlson, G. L. (1970). Hydroxylation of Polymethylsiloxane Surfaces by Oxidizing Plasmas. *Journal Applied Polymer Science, Vol. 14,* 2499-2508.

Jablonski, C. (2009). *Emerging Tech: LEGO toys and Shrinky Dinks aid in development of microfluidics.* Retrieved March 7, 2012, from http://www.zdnet.com/blog/emergingtech/lego-toys-and-shrinky-dinks-aid-in-development-of-microfluidics/1729

Koo, J. & Kleinstreuer, C. (2003). Liquid flow in microchannels: experimental observations and computer analyses of microfluidic effects. *Journal Micromech, Vol. 13,* 568.

Martinez, A. W., Phillips, S. T., & Whitesides, G. M. (2010). Diagnostics for the Developing World: Microfluidic Paper-Based Analytical Devices. *Analytical Chemistry, Vol. 82,* 3-10.

Murakami, T., Kuroda, S., & Osawa, Z. (1998). Dynamics of polymeric solid surfaces treated with oxygen plasma: effect of aging media after plasma treatment. *Journal Colloid and Interface Science*, *Vol. 202*, 37-44.

Owen, M. J. & Smith, P. J. (1994). Plasma treatment of poly (dimethyl) siloxane. *Journal Adhesion Science Technol.* , Vol. 8, 1063-1075.

Philips Analytical. (2008). *Basic XRF Spectrometry Tutorial.* CD.

Potts, P. J. (1986). X-ray fluorescence analysis: principles and practice of wavelength dispersive spectrometry. *A Handbook of Silicate Rock Analysis*, *Vol. 44*, 226-285.

Sia, S. K., & Whitesides, G. M. (2003). Microfluidic devices fabricated in poly(dimethylsiloxane) for biological studies. *Electrophoresis, Vol. 24*, 3563-3576.

Takayama, S. (2009). *Biological Application of Microfluidics.* Biomedical Engineering University of Michigan, PDF presentation. Retrieved April 6, 2012, from, http://www.lnf.umich.edu/index.php/SeminarDocs/4eea66b9-da25-4d48-834e-392fae3546c3.pdf

Tan, Y., Cristini, V., & Lee, A. P. (2005). Monodispersed Microfluidic Droplet Generation by Shear Focusing Microfluidic Device. *Sensors and Actuators B: Chemical*, *Vol. 114*, 350-356.

Tan, J., Li, S. W., Wang, K., & Luo, G.S. (2006). Controllable Preparation of Monodisperse O/W and W/O Emulsions in the Same Microfluidic Device. *Langmuir, Vol. 19,* 7943-7946.

Tan, J., Li, S. W., Wang, K., & Luo, G. S. (2009). Gas-Liquid Flow in T-Junction Microfluidic Devices With a New Perpendicular Rupturing Flow Route. *Chemical Engineering Journal*, *Vol. 146*, 428-433.

Tang, K. C., Liao, E., Ong, W. L., Wong, J. D. S., Agarwal, A., Nagarajan, R. & Yobas, L. (2006). Evaluation of bonding between oxygen plasma treated polydimethyl siloxane and passivated silicon. *Journal of Physics, Conference Series 34*, 155-161.

Teh, S., Lin, R., Hung, L., & Lee, A. P. (2008). Droplet Microfluidics. *Royal Society of Chemistry. Vol. 8*, 198-220.

Tice, J. D., Song, H., Lyon, A. D., & Ismagilov, R. F. (2003). Formation of Droplets and Mixing in Multiphase Microfluidics at Low Values of the Reynolds and the Capillary Numbers. *Langmuir, Vol. 19,* 9127-9133.

Tsuchida, M. & Osawa, Z. (1994). Effect of aging atmospheres on the changes in surface free energies of oxygen plasma-treated polyethylene films. *Colloid and Polymer Science, Vol. 272,* 770-776.

Unger, M. A., Chou H.P., Thorsen, T., Scherer, A., & Quake, S. R. (2000). Monolithic microfabricated valves and pumps by multilayer soft lithography. *Science, Vol. 288***,** 113-116.

Whitesides, G. M. (2006). The origins and the future of microfluidics. *NATURE, Vol. 442*, 368-372.

Xia, Y., & Whitesides, G. M. (1998). Soft lithography. *Angew. Chem. Int., Vol. 28*, 550-575.

Appendix

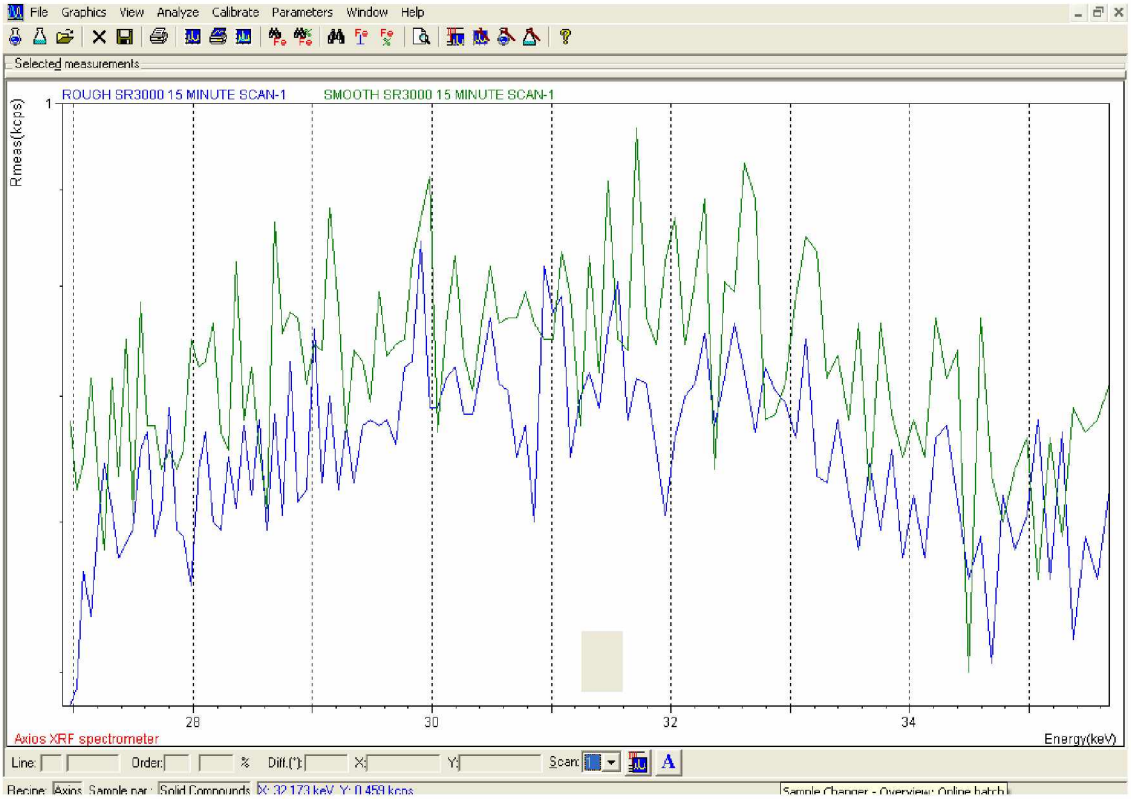

Figure 89: XRF Scan 1 data

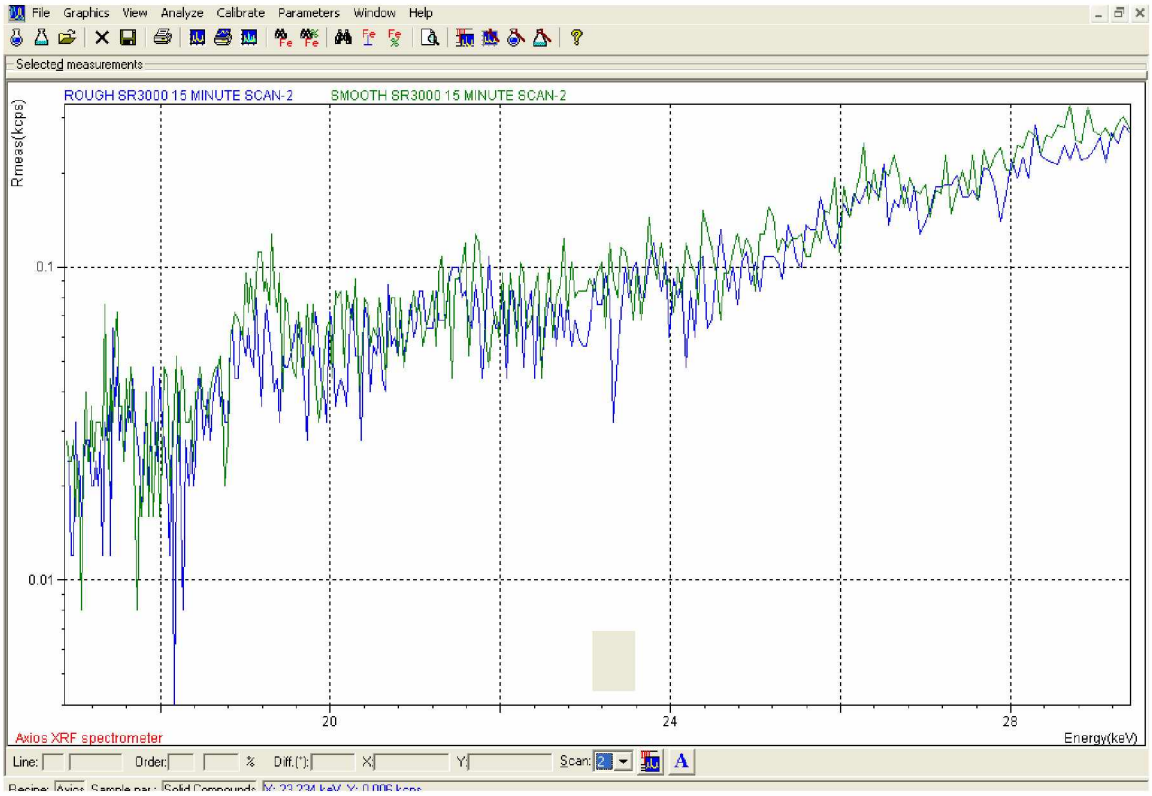

Figure 90: XRF Scan 2 data

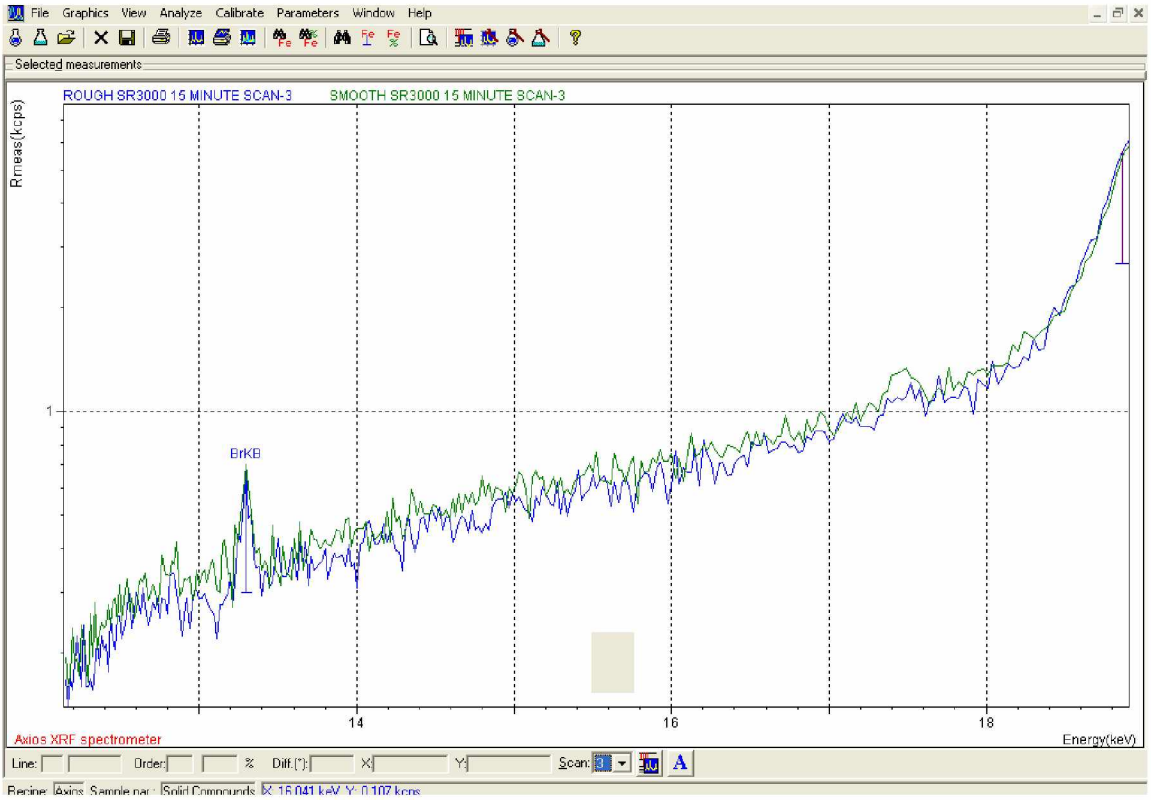

Figure 91: XRF Scan 3 data

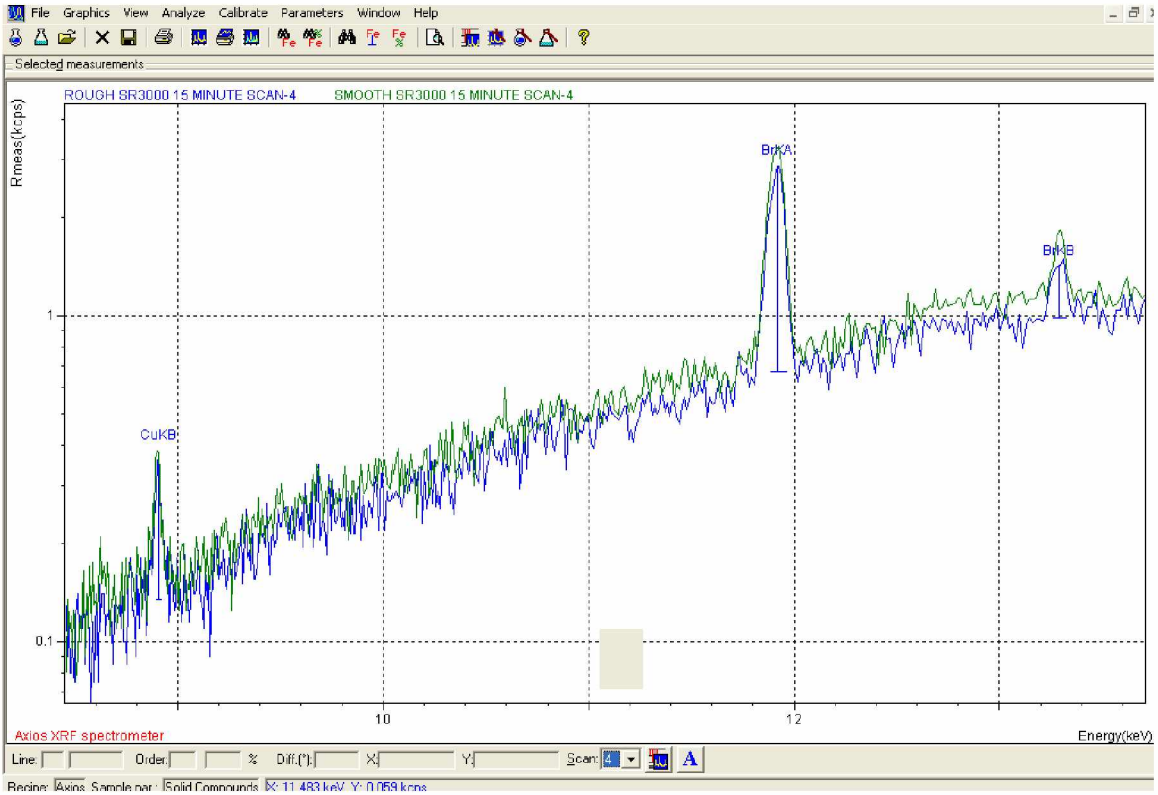

Figure 92: XRF Scan 4 data

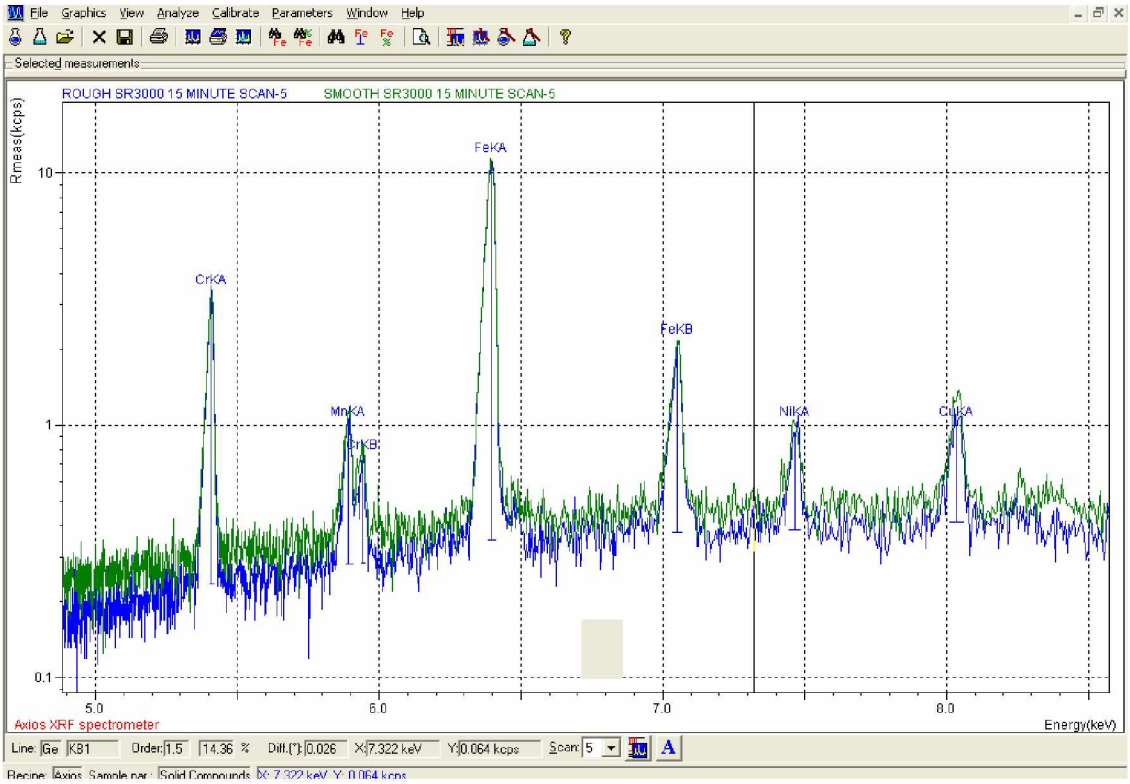

Figure 93: XRF Scan 5 data

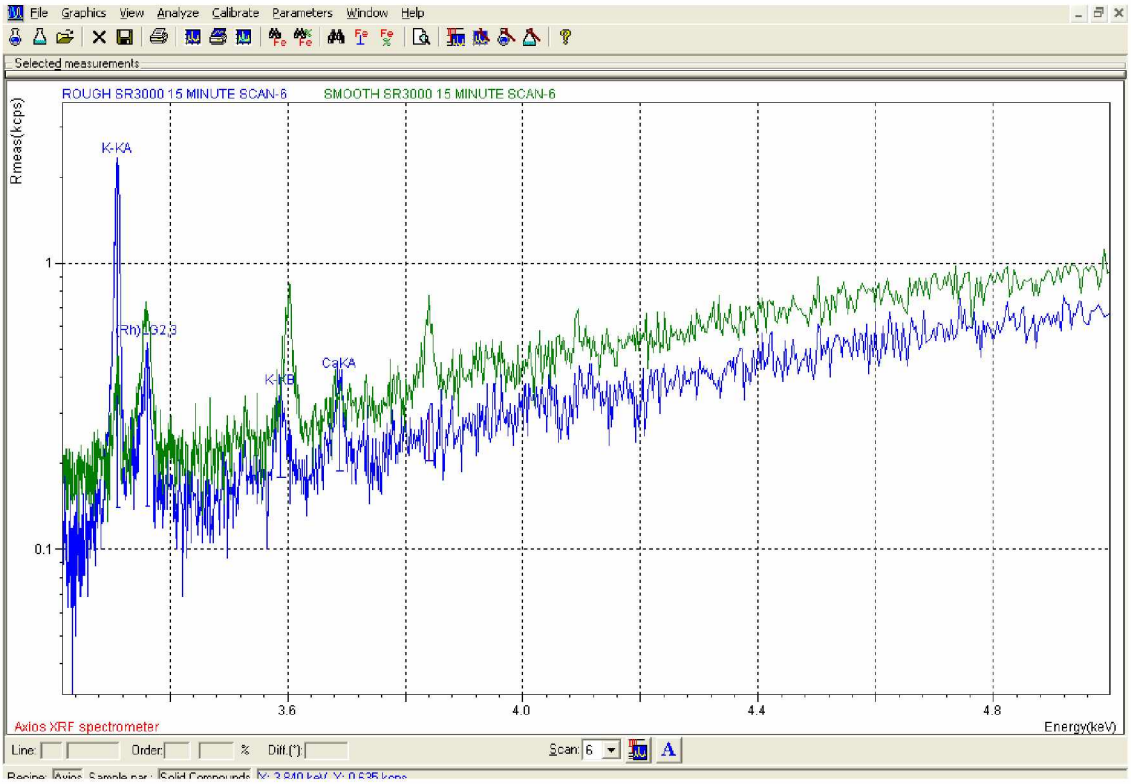

Figure 94: XRF Scan 6 data

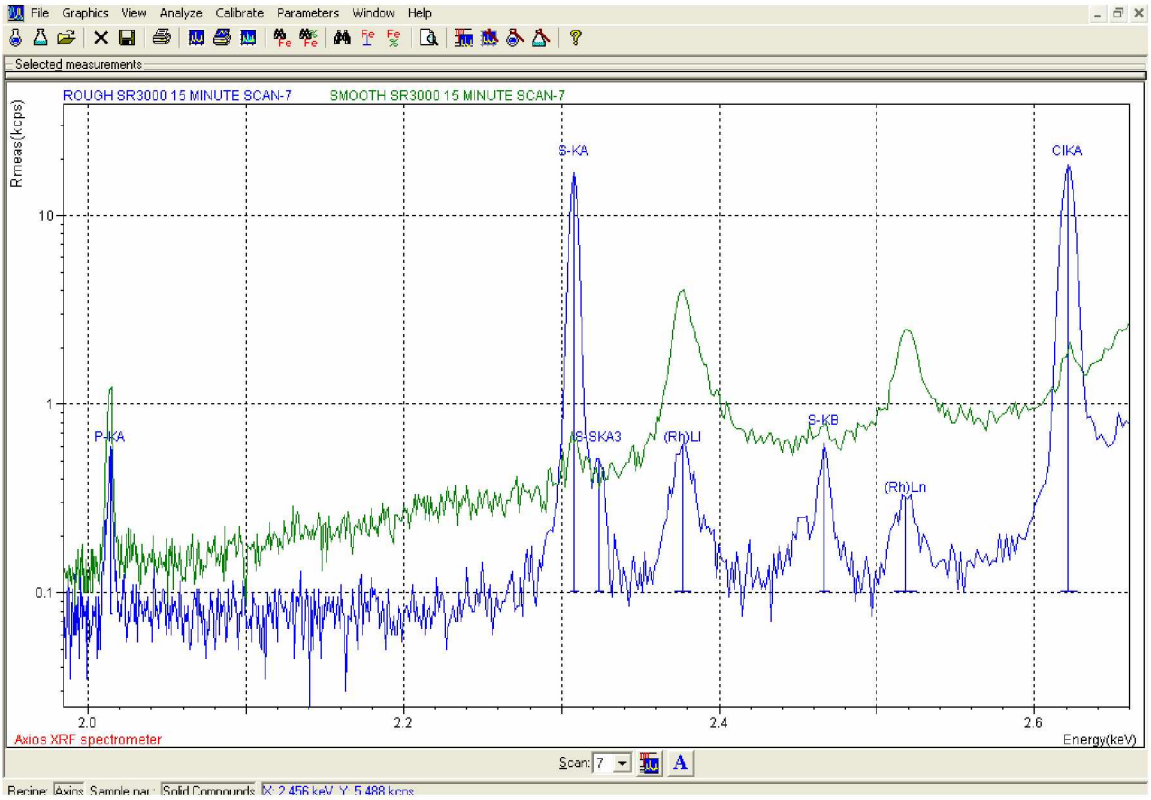

Figure 95: XRF Scan 7 data

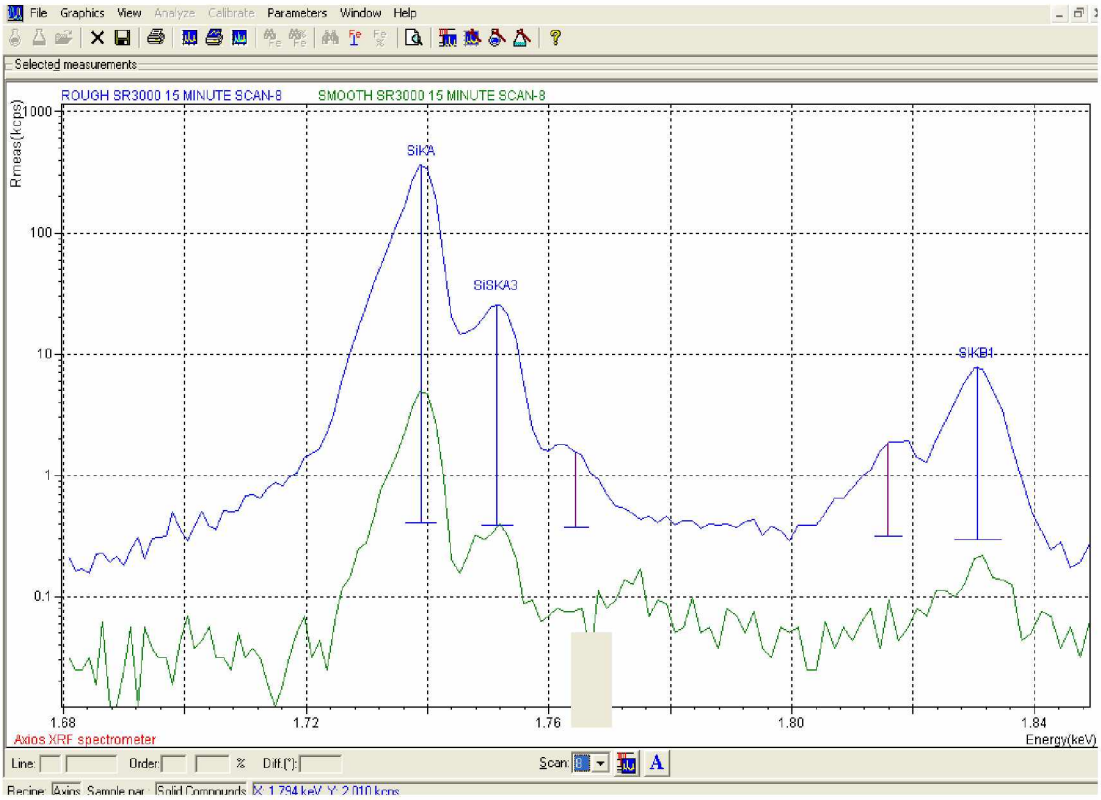

Figure 96: XRF Scan 8 data

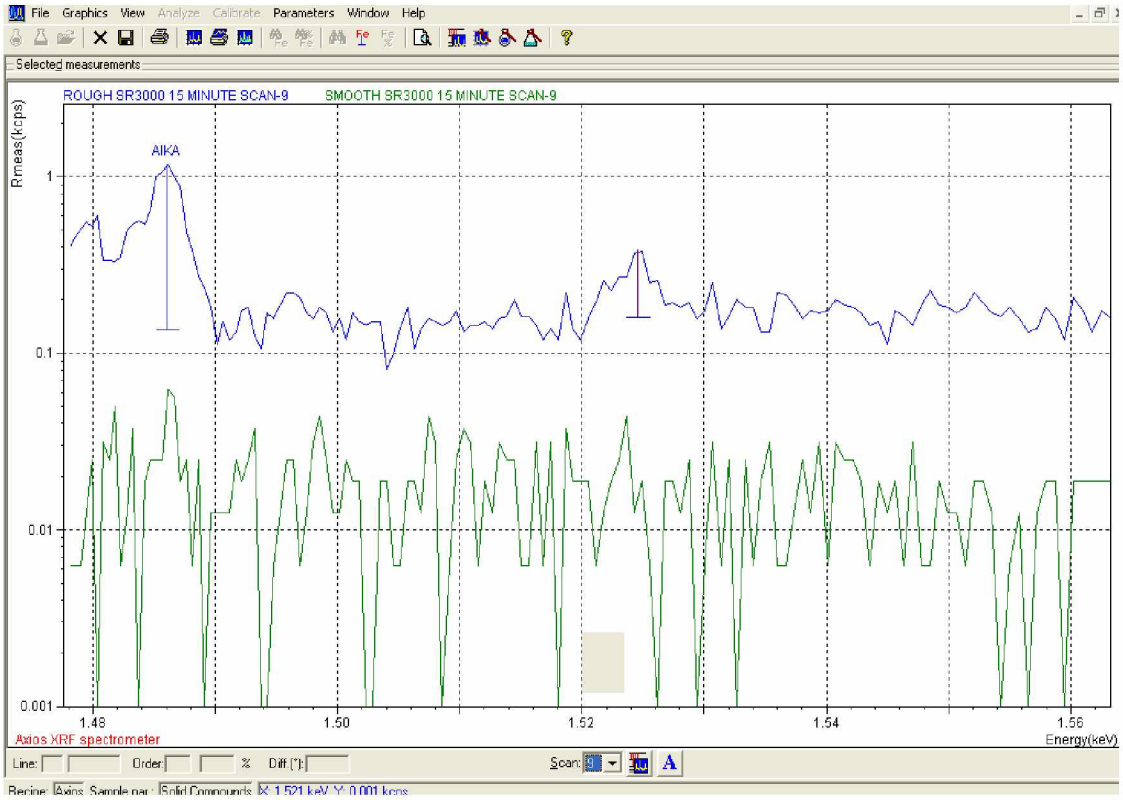

Figure 97: XRF Scan 9 data

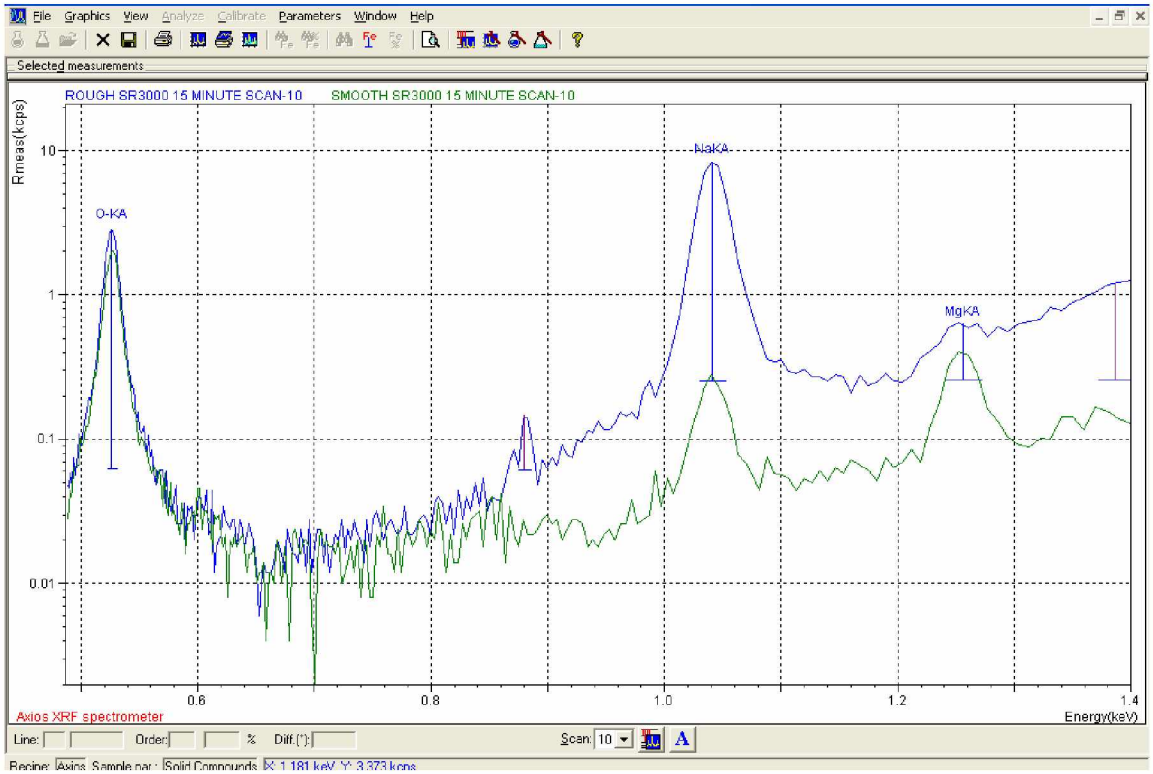

Figure 98: XRF Scan 10 data

Table 6: Plasma bonding strength results

Chamber Pressure (mTorr)	Power (Watts)	Treatment Time (s)	Rupture Pressure (psi)
200	LOW 6.8	20	21.47
		30	20.77
		40	20.00
		50	25.07
		60	24.37
		70	27.47
		80	26.13
		90	23.70
	MEDIUM 10.5	20	22.10
		30	22.00
		40	23.83
		50	20.43
		60	24.13
		70	22.27
		80	20.80
		90	19.73
	HIGH 18	20	47.53
		30	40.57
		40	54.70
		50	47.07
		60	41.27
		70	29.63
		80	22.90
		90	22.67
	LOW 6.8	20	49.60
		30	50.07
		40	36.23
		50	46.70
		60	35.97
		70	33.47
		80	23.37
		90	20.80
		20	22.47
		30	21.10

300	MEDIUM 10.5	40	21.20
		50	28.20
		60	25.27
		70	32.90
		80	24.70
		90	31.80
	HIGH 18	20	34.80
		30	32.57
		40	39.83
		50	29.57
		60	26.47
		70	27.60
		80	21.73
		90	36.20

Table 7: Contact angle date for zero and 30 seconds after placing on the surface

Chamber Pressure (mTorr)	Power (Watts)	Treatment Time (s)	Contact Angle (° Degrees) @ 0 seconds	Contact Angle (° Degrees) @ 30 seconds
200	LOW 6.8	20	80.73	72.33
		30	87.43	75.27
		40	92.23	83.83
		50	94.07	85.93
		60	94.77	86.63
		70	92.20	84.63
		80	87.33	80.50
		90	82.60	75.17
	MEDIUM 10.5	20	82.80	76.97
		30	82.80	74.77
		40	84.07	75.73
		50	88.67	80.27
		60	94.37	85.53
		70	93.77	84.33
		80	91.23	83.00
		90	87.27	80.23
		20	72.43	66.83
		30	75.40	68.80

	HIGH 18	40	76.77	70.07
		50	81.20	74.07
		60	78.00	70.47
		70	70.57	66.00
		80	63.17	60.83
		90	57.53	55.40
300	LOW 6.8	20	65.93	63.53
		30	75.47	75.03
		40	86.90	80.60
		50	89.20	84.80
		60	89.30	83.23
		70	87.33	85.20
		80	78.50	83.07
		90	72.97	73.07
	MEDIUM 10.5	20	60.73	58.17
		30	63.00	59.50
		40	76.60	73.43
		50	82.00	76.83
		60	89.50	80.63
		70	102.20	91.37
		80	97.90	90.87
		90	92.23	85.83
	HIGH 18	20	56.23	53.60
		30	62.03	60.03
		40	66.03	63.67
		50	79.60	75.07
		60	88.57	81.70
		70	87.37	79.73
		80	76.17	74.07
		90	70.33	65.97